

Low Temperature Laboratory

# Dynamics of Quantized Vortices in Applied Flow in Superfluid $^3\text{He-B}$

---

Robert Jan de Graaf



# Dynamics of Quantized Vortices in Applied Flow in Superfluid $^3\text{He-B}$

**Robert Jan de Graaf**

Doctoral dissertation for the degree of Doctor of Science in  
Technology to be presented with due permission of the School of  
Science for public examination and debate in Auditorium AS1 at the  
Aalto University School of Science (Espoo, Finland) on the 18<sup>th</sup> of  
May 2011, at 12 o'clock noon.

**Aalto University  
School of Science  
Low Temperature Laboratory  
ROTA Group**

**Supervisor**

Prof.Dr. M. Kaivola

**Instructor**

Prof.Dr. M. Krusius

**Preliminary examiners**

Prof.Dr. V.V. Dmitriev, Kapitza Institute for Physical Problems, Russia

Prof.Dr. E.V. Thuneberg, University of Oulu, Finland

**Opponent**

Prof.Dr. S.N. Fisher, Lancaster University, United Kingdom

Aalto University publication series

**DOCTORAL DISSERTATIONS 37/2011**

© Robert Jan de Graaf

ISBN 978-952-60-4108-7 (pdf)

ISBN 978-952-60-4107-0 (printed)

ISSN-L 1799-4934

ISSN 1799-4942 (pdf)

ISSN 1799-4934 (printed)

Aalto Print

Helsinki 2011

The dissertation can be read at <http://lib.tkk.fi/Diss/>

**Author**

Robert Jan de Graaf

**Name of the doctoral dissertation**

Dynamics of Quantized Vortices in Applied Flow in Superfluid  $^3\text{He-B}$

**Publisher** School of Science

**Unit** Low Temperature Laboratory

**Series** Aalto University publication series DOCTORAL DISSERTATIONS 37/2011

**Field of research** Condensed Matter Physics

**Manuscript submitted** 4 March 2011

**Manuscript revised** 11 April 2011

**Date of the defence** 18 May 2011

**Language** English

**Monograph**

**Article dissertation (summary + original articles)**

This thesis is mostly focussed on studies of dynamics of superfluid  $^3\text{He-B}$  at temperatures below  $0.4T_c$  where the flow of quantized vortex lines was expected to be generally turbulent. The damping in vortex motion changes many orders of magnitude in a small temperature interval making vortices in superfluids an ideal tool to study turbulence. The quantum nature of vortices in superfluids allows for exotic hydrodynamics that does not exist in classical fluids. Earlier research had showed that vortices become unstable and lead to turbulence when the superfluid Reynolds number exceeds unity. The question remained open whether vortical flow is inherently unstable at lower temperatures. This thesis addresses issues surrounding the instability of quantized vortices in applied flow in the zero-temperature limit. Using the non-invasive nuclear magnetic resonance measurement technique, we have studied the dynamics of vortices in transient states during spin-up experiments where the rotation velocity of the system changes in a step-like manner. We found transition temperatures where the vortices connected to the cylindrical container become unstable and, ultimately, start a turbulent burst of vortex formation. This is in contrast to the laminar motion at higher temperatures, where the vortex ends smoothly slide in helical motion on the cylindrical surface. The exact conditions for this onset temperature to turbulence are established in terms of the applied flow, and the perturbation of the superfluid state by so-called seed vortices. The spin-up and spin-down experiments in the zero-temperature limit show different vortex dynamics. The vortex motion in applied flow is laminar for a cylindrical container, while in a cubical geometry the motion is expected to be partly turbulent. Our experiments on turbulent front propagation after injection of seed vortices from the AB-phase boundary (via the Kelvin-Helmholtz instability) into the rotating Landau state show a change over from quasi-classical turbulence at high temperatures, to quantum turbulence in the low temperature regime where the energy cascade of Kelvin wave excitations starts to contribute to the dissipative process. The effect of a bottleneck in this energy cascade is expressed in the front propagation velocity. The contribution of the density anisotropy to the textural energy of the superfluid in rotation is measured from the high to the zero-temperature limit. Comparison with theory allows determination of the superfluid energy gap. We have mapped the superfluid order parameter flare out textures in terms of applied flow and temperature. A quartz tuning fork with a high quality factor has been studied in superfluid  $^3\text{He-B}$ . The device is found to be an excellent tool to measure temperature, pressure and viscosity. In the zero-temperature limit, where other temperature measurement devices start to saturate, the fork's sensitivity increases due to the exponential dependence on the quasiparticle density.

**Keywords** Superfluids, helium, vortex dynamics, front propagation, laminar, turbulence, Reynolds number, nuclear magnetic resonance, quartz tuning fork

**ISBN (printed)** 978-952-60-4107-0

**ISBN (pdf)** 978-952-60-4108-7

**ISSN-L** 1799-4934

**ISSN (printed)** 1799-4934

**ISSN (pdf)** 1799-4942

**Location of publisher** Espoo

**Location of printing** Helsinki

**Year** 2011

**Pages** 51

**The dissertation can be read at** <http://lib.tkk.fi/Diss/>



## Acknowledgments

I want to thank all the people that inspired, motivated, and helped me to accomplish my doctoral studies.

My gratitudes are expressed towards Prof. Mikko Paalanen, for giving me the opportunity to work at the Low Temperature Laboratory. I especially want to thank Prof. Matti Krusius for accepting me in the ROTA group and for his guidance in the exciting field of experimental physics. My gratitude to Vladimir Eltsov (current head of the group) is great. His broad and deep understanding in experimental as well as in theoretical physics is inspiring. Computational work by Juha Kopu and Risto Hänninen is much appreciated and invaluable for the interpretation of our measured data. Antti Finne and Rob Blaauwgeers taught me the operations of the rotating cryostat and I thank both for their support during my first months in the ROTA group. The help of Roman Solntsev in the preparation and the recovery of the cryostat is much appreciated. Jaakko Hosio's analysis of the fork data and the construction of the NMR setup by Petri Heikkinen have substantial weight in the work presented here. Both are gracious colleagues. The guidance and advice of Matti Kaivola has been very helpful at the last stages of this thesis.

I am grateful for the theoretical support by E.V. Thuneberg, G.E. Volovik and N.B. Kopnin. Their contributions to the work are invaluable. I want to thank V.S. L'vov, A.I. Golov, P.M. Walmsley, G.R. Pickett, R.P. Haley, P. Skyba, L. Skrbek, M. Tsubota, H. Yano, and W. Schoepe for their collaborative work in the research of quantum turbulence. Their visits to the Helsinki group is much appreciated. Visiting graduate students D.E. Zmeev, D. Schmoranzner, P. Hunger, T.V. Chagovets and M. Človečko have been helpful and their presence enjoyable.

I want to thank the administrative and the technical staff for all their effort: P. Berglund, Pirjo Muukkonen, Olga Jakkola, Susanna Jauhiainen, Teija Halme, Helena Hellström, Tuire Koivisto, Liisi Pasanen, Kirsi Romanoff, A. Savin and Katariina Toivonen. The craftsmen of the workshop made the many precious parts: S. Hiltunen, A. Isomäki, S. Kaivola, H. Kaukulin and in particular M. Korhonen. The network/computer support team (the wizards) have been great colleagues and gave great technical support: H. Junes, M. Laakso, P. Räisänen, R. Schreiber and P. Virtanen. Fellow graduate students Anssi Salmela, Juho Rysti, Matti Manninen and many others made the laboratory a convivial place to work.

Finally I would like to express my gratitude and love to Esther for her courage, patience and trust in our relationship at times when the physical distance was large and time passed slowly. The love of my mother Corry has always been unconditional, warm and supportive.

Otaniemi, April 2011

Robert Jan de Graaf

## List of publications

The list is ordered by the author's contribution, and significance.

- [P1] R. de Graaf, V.B. Eltsov, P.J. Heikkinen, J.J. Hosio, R. Hänninen and M. Krusius, *Textures of superfluid  $^3\text{He-B}$  in applied flow and comparison with hydrostatic theory*, J. Low Temp. Phys., 25 pages (Accepted February 16, 2011). Copyright © 2011 Springer Science and Business Media.  
Measurements on the order parameter texture are compared with numerical calculations using the Hydrostatic Theory of  $^3\text{He-B}$ . The work on the analysis of the NMR spectrum concentrates on the density anisotropy parameter in applied flow and the textural transitions. A new spin wave resonance is identified.
- [P2] V.B. Eltsov, R. de Graaf, P.J. Heikkinen, J.J. Hosio, R. Hänninen, M. Krusius and V.S. L'vov, *Stability and dissipation of laminar vortex flow in superfluid  $^3\text{He-B}$* , Phys. Rev. Lett. **105**, 125301 1-4 (2010). Copyright © 2010 American Physical Society  
Report on the stability of laminar vortex flow at superfluid Reynolds numbers significantly larger than unity. The spin-up and spin-down dynamics of the superfluid component is laminar down to the temperature of  $0.2 T_c$ , where the superfluid Reynolds number is  $Re_\alpha \sim 10^3$ .
- [P3] V.B. Eltsov, A.I. Golov, R. de Graaf, R. Hänninen, M. Krusius, V.S. L'vov and R.E. Solntsev, *Quantum turbulence in a propagating superfluid vortex front*, Phys. Rev. Lett. **99** (26), 265301 1-4 (2007). Copyright © 2007 American Physical Society.  
The study of a vortex front propagating into the vortex-free Landau state shows at low temperatures a dissipation anomaly, which is expressed by the front velocity. At about  $0.3 T_c$  the energy transfer to the Kelvin-wave cascade is strongly suppressed by a bottleneck effect.
- [P4] R. de Graaf, R. Hänninen, T.V. Chagovets, V.B. Eltsov, M. Krusius and R.E. Solntsev, *The dynamics of vortex generation in superfluid  $^3\text{He-B}$* , J. Low Temp. Phys. **153** (5-6), 197-227 (2008). Copyright © 2008 Springer Science and Business Media.  
Report on the rapid decrease in the damping of vortex motion with decreasing temperature and its consequences to the dynamics. Below a temperature of  $0.6 T_c$  expanding vortices become unstable in externally applied flow, reconnect on the container surface, create new vortices and ultimately give rise to a turbulent burst.
- [P5] V.B. Eltsov, R. de Graaf, P.J. Heikkinen, J.J. Hosio, R. Hänninen and M. Krusius, *Vortex formation and annihilation in rotating superfluid  $^3\text{He-B}$  at low temperatures*, J. Low Temp. Phys. **161**, 474-508 (2010). Copyright © 2010 Springer Science and Business Media.  
Detailed report on the stability of laminar vortex flow in a rapid change of rotation in a cylindrically symmetric environment. At temperatures which reflect the superfluid properties in the  $T \rightarrow 0$  regime, the global vortex motion is laminar with only a thin turbulent layer adjacent to the cylindrical surface.

- [P6] R.E. Solntsev, R. de Graaf, V.B. Eltsov, R. Hänninen and M. Krusius, *Dynamic remanent vortices in superfluid  $^3\text{He-B}$* , J. Low Temp. Phys. **148** (3-4), 311-316 (2007). Copyright © 2007 Springer Science and Business Media.  
The annihilation of remanent vortices after a deceleration of the rotation velocity to zero has been studied. With decreasing temperature, the survival time increases rapidly. Re-applying rotation shows that above the temperature of  $0.6 T_c$  the vortex number is conserved, while below  $0.55 T_c$  vortices are unstable, which ultimately gives rise to a turbulent burst.
- [P7] R. Hänninen, V.B. Eltsov, A. Finne, R. de Graaf, J. Kopu, M. Krusius and R.E. Solntsev, *Precessing vortex motion and instability in a rotating column of superfluid  $^3\text{He-B}$* , J. Low Temp. Phys. **155** (1), 98-113 (2009). Copyright © 2009 Springer Science and Business Media.  
Report on the study of the propagation of newly formed vortices in a cylindrical container close to the onset temperature  $T_{\text{on}}$  to turbulence. An instability of a single expanding vortex results in slow vortex multiplication. The helically precessing motion of a vortex bundle is observed with NMR.
- [P8] R. Blaauwgeers, M. Blažková, M. Človečko, V.B. Eltsov, R. de Graaf, J.J. Hosio, M. Krusius, D. Schmoranzner, W. Schoepe, L. Skrbek, P. Skyba, R.E. Solntsev and D.E. Zmeev, *Quartz tuning fork: Thermometer, pressure- and viscometer for helium liquids*, J. Low Temp. Phys. **146** (5-6), 537-562 (2007). Copyright © 2007 Springer Science and Business Media.  
Mechanical properties of quartz tuning forks with a high quality factor are explored in the regime of linear viscous hydrodynamics in normal and superfluid  $^3\text{He}$  and  $^4\text{He}$ . The measurements are compared to the hydrodynamic model of the sensor.
- [P9] M. Blažková, M. Človečko, V.B. Eltsov, E. Gažo, R. de Graaf, J.J. Hosio, M. Krusius, D. Schmoranzner, W. Schoepe, L. Skrbek, P. Skyba, R.E. Solntsev and W.F. Vinen, *Vibrating quartz fork - A tool for cryogenic helium research*, J. Low Temp. Phys. **150** (3-4), 525-535 (2008). Copyright © 2008 Springer Science and Business Media.  
Quartz tuning forks with a high quality factor can be used as thermometer, pressure- and viscometer. Their potential use as generators and detectors of cavitation and turbulence in viscous and superfluid He liquids is explored.
- [P10] V.B. Eltsov, R. de Graaf, R. Hänninen, M. Krusius and R.E. Solntsev, *Experiments on the twisted vortex state in superfluid  $^3\text{He-B}$* , J. Low Temp. Phys. **150** (3), 373-383 (2008). Copyright © 2008 Springer Science and Business Media.  
Experiments on the propagating front and on the trailing twisted vortex bundle are compared with numerical simulations. Towards high temperatures, the thickness of the front increases while in the low temperature regime the thickness is constant. The increasing twist at low temperatures is limited by the reconnection of vortices.

- [P11] V.B. Eltsov, R. de Graaf, M. Krusius and D.E. Zmeev, *Vortex core contribution to textural energy in  $^3\text{He-B}$  below  $0.4T_c$* , J. Low Temp. Phys. **162**, 212-225 (2011).  
Copyright © Springer Science and Business Media, LLC 2010

The vortex core contribution to the textural energy is measured by tracking the magnon condensate states in a trap formed by the order parameter. The gyromagnetic effect, i.e. the difference in measurements when the vortices are parallel or antiparallel with the axially oriented magnetic field, is observed in the low temperature range.

## Author's contribution

The work in this thesis is experimental and has been performed in the ROTA group of the Low Temperature Laboratory during the years 2005-2010. In 2005 the author started his work at the moment when the cryostat was undergoing reconstruction with the goal of reaching lower temperatures. The author contributed to the installation of a second co-rotating platform for the measurement equipment which reduced the heat leaks substantially and made rotating measurements possible below  $0.3 T_c$ . The first cool down of the newly born cryostat took place in autumn 2005. Handling, operating and repairs of the rotating cryostat is a team effort and was equally distributed between the 3-5 researchers present in the group, with emphasis on the distribution of skills. Changes made by the author on the cryostat include the implementation of an optical encoder to mechanically de-couple the second co-rotating platform and changes to the NMR resonance circuit. The author's contribution in the movement of the cryostat to a new laboratory building is significant. This provided an unique opportunity to learn the many complex aspects of the cryostat's design.

The work of publication [P1] is fully attributed to the author: the measurements, detailed analysis and the writing of the paper. The publication is an extensive study of the order parameter texture of rotating superfluid  $^3\text{He-B}$  in the zero-temperature limit. NMR spectra are quantitatively compared with calculations using the Hydrostatic Theory of  $^3\text{He-B}$ . Part of the experimental result is the ability to predict the NMR spectra of the superfluid flow with a varying number of vortices, down to the lowest temperatures.

The work on extracting the vortex density from NMR spectra has played a crucial role in the author's analysis of the spin-up and spin-down experiments where the vortex dynamics turned out to be laminar, and not turbulent. This result was unexpected. The experiments were repeated using a different methodology for the determination of the vortex density, and took place in another cylinder. The initial claim held and the experimental data measured and analyzed by the author resulted in the publication in Phys. Rev. Lett. [P2].

The author's contributions to the experimental results in the remaining publications [P3-P9] are in the preparation of the experiment and the analysis concerning the relation between the measured spectra and the vortex density in the observed processes around the onset temperature to turbulence. The latter is fully attributed to the author. In particular the statistical analysis of the vortex formation experiments published in [P4], and of the annihilation processes in publication [P5] were carried out by the author. The author's contribution to [P10-11] lies solely in the preparation of the experiments.

# Contents

<b>Acknowledgments</b>	<b>i</b>
<b>List of publications</b>	<b>ii</b>
<b>Author's contribution</b>	<b>v</b>
<b>1 Introduction</b>	<b>1</b>
1.1 Superfluid $^3\text{He}$ and $^3\text{He-B}$ . . . . .	2
1.2 Hydrostatic theory of $^3\text{He-B}$ . . . . .	3
1.3 Nuclear magnetic resonance . . . . .	4
1.4 Vortex lines in $^3\text{He-B}$ . . . . .	6
1.5 Classical and quantum turbulence . . . . .	9
<b>2 Experimental setup</b>	<b>12</b>
2.1 Rotating cryostat . . . . .	12
2.2 Nuclear magnetic resonance setup . . . . .	14
<b>3 Quartz tuning forks in superfluid <math>^3\text{He}</math></b>	<b>18</b>
3.1 Mechanical properties and hydrodynamics . . . . .	18
3.2 Tuning fork response in the linear regime . . . . .	20
3.3 Andreev reflection from a vortex tangle . . . . .	22
<b>4 Textural energies and NMR spectra</b>	<b>25</b>
4.1 Flare out textures of $^3\text{He-B}$ in applied flow . . . . .	25
4.2 Counterflow and density anisotropy . . . . .	28
<b>5 Vortex dynamics in superfluid <math>^3\text{He-B}</math></b>	<b>33</b>
5.1 Preparing the Landau state in rotation . . . . .	33
5.2 Vortex formation in applied flow . . . . .	33
5.3 Vortex annihilation . . . . .	37
5.4 Propagating superfluid vortex front . . . . .	40
<b>6 Conclusions</b>	<b>44</b>
<b>Appendix</b>	<b>46</b>

# 1 Introduction

The research on the dynamics of topological objects in superfluid  $^3\text{He}$  has been an ongoing long term goal of the ROTA group. The work presented in this thesis started with a particular interest in the dynamics of vortices in the low temperature limit where the superfluid was expected to express turbulent behaviour under most conditions of strong externally applied flow. Unlike turbulence in classical fluids, the vorticity in superfluids is quantized. The mutual friction in superfluid  $^3\text{He-B}$ , which controls the damping of the vortex motion, changes more than three orders of magnitude in a small temperature regime. The dynamics of vortices under applied rotating flow had been studied earlier at relatively high temperatures, but the zero-temperature limit was not explored until now. In this regime, the contribution to the viscosity by the normal component vanishes and the question arises how this affects the dynamics of vortices. This thesis answers this question with the presentation of an unexpected result.

In this chapter we start with the hydrostatic theory of superfluid  $^3\text{He-B}$ . The terms contributing to free energy of the order parameter texture are listed. These are needed later for the interpretation of measured and calculated spectra. The section on NMR shows how the texture can be probed non-invasively. The theory is expanded by introducing vortices and we show the dynamics of a single vortex line in a rotating cylindrical container. Flow profiles of the superfluid are given for different vortex cluster configurations. The chapter is concluded with a description of turbulent behaviour of quantized vortices.

The second chapter discusses the rotating cryostat and the experimental arrangement for the NMR setup. The focus is on the improvements of the cryostat which enabled us to reach the low temperature regime down to  $0.2 T_c$ .

Our contribution to the research of quartz tuning forks deserved its own chapter. The properties of this mechanical resonator with a high quality factor are discussed both in vacuum as well as in normal and superfluid  $^3\text{He}$ . The response of the fork is shown from the relatively high temperature of 50 mK down to 0.44 mK. The sensitivity of the fork is demonstrated by a bolometric measurement of the heat release from NMR absorption and an experiment showing Andreev reflection of quasiparticles on a vortex tangle.

Chapter 4 reports on the analysis of NMR spectra on rotating superfluid with a variation of vortex clusters. The measurements not only provided a calibration of the vortex number from a NMR absorption peak, but also allowed for a comparison with hydrostatic theory. The calibration can now be used to analyze transients in vortical flow. The analysis of the NMR spectra as a function of the azimuthal counterflow velocity also provides a fit of the density anisotropy and thereby of the superfluid energy gap.

Chapter 5 addresses the question of the dynamics of vortices in the zero-temperature limit. The formation of vortices in applied flow is discussed in a variety of scenarios, ranging from the single vortex multiplication process to an injection of a bundle of vortices directly into the Landau state. The reverse, vortex annihilation, is discussed for spin-down experiments where the relaxation of the vortex cluster is monitored when the rotation is abruptly stopped. We conclude the section with a detailed study on the propagating turbulent vortex front which is a major constituent of the complex process by which the vortex-free Landau state is replaced by the equilibrium rotating vortex state.

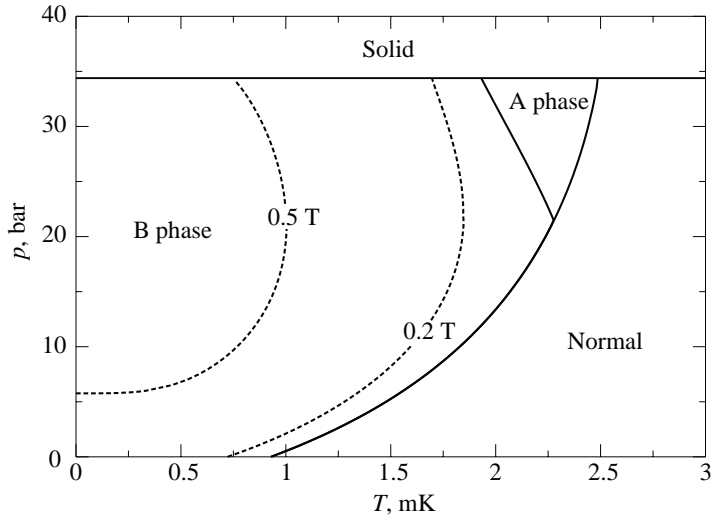


Figure 1: The phase diagram of  $^3\text{He}$ . Below the melting curve at  $p \approx 34$  bar liquid  $^3\text{He}$  is either superfluid or a normal viscous fluid. The transition at  $T_c$  (pressure-dependent) from the normal fluid (Fermi-liquid theory) into a superfluid (BCS theory) is of second order. At high pressures and high temperatures and zero external magnetic field, the A-phase is favoured, while at low temperatures the B-phase is the ground state. The AB-phase transition is of first order. By applying an external magnetic field the AB-phase transition is moved to lower temperatures.

## 1.1 Superfluid $^3\text{He}$ and $^3\text{He-B}$

The first inert element in the periodic system is Helium, which can exist as two stable isotopes:  $^3\text{He}$  and  $^4\text{He}$ . While the two only differ in one neutron in the nucleus, the hydrodynamic properties of the superfluids at low temperature are very distinct due to the involved quantum-statistics:  $^3\text{He}$  atoms are fermions, while  $^4\text{He}$  atoms are bosons. In this work we concentrate on the  $^3\text{He}$  isotope. At the temperature of  $T = 3.2$  K,  $^3\text{He}$  condenses into a liquid at the pressure of  $p = 1$  bar. Down to  $\sim 0.1$  K the fluid is described by classical fluid theory, while below this temperature the fluid description comes from Fermi-liquid theory [1]. At temperatures  $1 \div 2.5$  mK, the  $^3\text{He}$  fluid becomes a superfluid. See Fig. 1 for the pressure dependence of the critical temperature  $T_c$  of the superfluid transition.

Superfluidity in  $^3\text{He}$  liquid emerges through the Cooper pairing of two  $^3\text{He}$  atoms, similar to how superconductivity appears in a superconductor as described by BCS theory [2]. In the  $^3\text{He}$  superfluid the hard-core repulsion in the inter-atomic potential forces the Cooper pairing to occur in the orbital triplet state ( $L = 1$ ), leading to a  $3 \times 3$  complex order parameter matrix  $A_{\mu\nu}$ , where the first index refers to the spin and the second to orbital degrees of freedom. Three stable bulk phases exist in the superfluid  $^3\text{He}$ : A, B and  $A_1$ . See the temperature, pressure and field dependent phase diagram in Fig. 1.

The A-phase is the Anderson-Brinkman-Morel (ABM) state [3]. Here the Cooper pairing is formed by aligning the spins, with spin projection  $S_z = \pm 1$  ( $|\uparrow\uparrow\rangle$  and  $|\downarrow\downarrow\rangle$ ) states. This phase is not considered in this thesis, since our measurements are in the low temperature regime at low magnetic fields.

The B-phase is the Balian-Werthamer (BW) state [4]. This is the preferred state at low magnetic field and low temperatures. Here the projected spin state is  $S_z = 0, \pm 1$ . The order parameter describing the structure of the superfluid, can be written as [5]

$$A_{\mu\nu} = \Delta(T)R_{\mu\nu}(\hat{n}, \theta)e^{i\phi}, \quad (1)$$

with  $\Delta(T)$  the temperature-dependent energy-gap,  $\phi$  the condensate's phase, and  $R_{\mu\nu}$  the rotation matrix describing the rotation of the spin and orbital coordinates relative to each other by the angle  $\theta$  around the axis oriented along the unit vector  $\hat{n}$ :

$$R_{\mu\nu}(\hat{n}, \theta) = \cos\theta\delta_{\mu\nu} + (1 - \cos\theta)\hat{n}_\mu\hat{n}_\nu - \sin\theta\epsilon_{\mu\nu k}\hat{n}_k. \quad (2)$$

Due to the spin-orbit interaction, the dipolar energy is in equilibrium when the angle  $\theta = \arccos(-\frac{1}{4})$ . The unit vector  $\hat{n}$  can be specified with the azimuthal angle  $\alpha$  and the polar angle  $\beta$ . The orientation of the  $\hat{n}$ -vector over real space is called the *texture*.

## 1.2 Hydrostatic theory of $^3\text{He-B}$

The textural anisotropy arises from small residual interactions which distort the spherical symmetry of the orbital or spin spaces, such as the applied magnetic field  $H$  [6]. The texture of the orbital anisotropy axis  $\hat{l} = (\vec{H}/H)R(\hat{n}, \theta)$  prefers  $\hat{l} \parallel \vec{H}$ , while the walls of a container orient  $\hat{l}$  perpendicular to themselves. The magnetic field  $H$  gives rise to the magnetic orientational free energy term

$$F_{\text{DH}} = -a \int d^3r (\hat{n} \cdot \vec{H})^2, \quad (3)$$

while the relative flow of the superfluid and normal fractions leads to a dipole flow velocity term

$$F_{\text{DV}} = -\lambda_{\text{DV}} \int d^3r [\hat{n} \cdot (\vec{v}_s - \vec{v}_n)]^2. \quad (4)$$

Here  $\vec{v}_s - \vec{v}_n$  is the counterflow velocity between the superfluid and normal component as described by the two fluid model (see section 1.4). The stiffness of the order parameter is reflected by the gradient term

$$F_{\text{G}} = \int d^3r \left[ \lambda_{\text{G1}} \frac{\partial R_{\alpha i}}{\partial r_i} \frac{\partial R_{\alpha j}}{\partial r_j} + \lambda_{\text{G2}} \frac{\partial R_{\alpha j}}{\partial r_i} \frac{\partial R_{\alpha j}}{\partial r_i} \right], \quad (5)$$

which arises from the coherence of the superfluid state: rapid spatial changes are suppressed. The anisotropy axis  $\hat{l}$  prefers to align with the direction of the counterflow  $\vec{v}_n - \vec{v}_s$ , which changes the direction of the anisotropy axis of the energy gap  $\Delta$ . The associated energy is the field velocity term

$$F_{\text{HV}} = -\lambda_{\text{HV}} \int d^3r \left[ \vec{H} \cdot \overleftarrow{R} \cdot (\vec{v}_s - \vec{v}_n) \right]^2. \quad (6)$$

At the surface, the contribution to the surface energy arises from the suppression of those pairing interactions where the orbital angular momentum is oriented parallel to the wall. Here we assume that the curvature of the surface is small and that the length scale of the distortion, the superfluid coherence length  $\xi(T)$ , is small compared to the dipole healing length  $\xi_D$ . The latter is obtained by equating the energy density associated with a particular orienting force to the bending energy density. The surface gives rise to the surface field term

$$F_{\text{SH}} = -d \int_{\text{S}} d^2r (\vec{H} \cdot \overleftarrow{R} \cdot \hat{e}_s^2). \quad (7)$$

Here the unit vector  $\hat{e}_s$  is perpendicular to the surface and points towards the superfluid. We refer to formulas (35)...(40) in Ref. [7] for the parameters  $a$ ,  $\lambda_{\text{DV}}$ ,  $\lambda_{\text{G1}}$  and  $\lambda_{\text{G2}}$ . The temperature-dependent field velocity parameter

$$\lambda_{\text{HV}} = \frac{\rho}{\Delta^2} \frac{m^*/m}{(1 + \frac{1}{3}F_1^s Y)^2} \left[ \frac{\frac{1}{2}\hbar\gamma\mu_0(1 + \frac{1}{5}F_2^a)}{1 + F_0^a(\frac{2}{3} + \frac{1}{3}Y) + \frac{1}{5}F_2^a(\frac{1}{3} + (\frac{2}{3} + F_0^a)Y)} \right]^2 \times \left[ Z_3 - \frac{9}{10}Z_5 + \frac{9}{10}\frac{Z_5^2}{Z_3} - \frac{3}{2}Z_7 + \frac{3F_2^a Z_3}{50(1 + \frac{1}{5}F_2^a)}(3Z_5 - 2Z_3) \right] \quad (8)$$

expresses the magnitude of the density anisotropy of the superfluid along  $\hat{l}$ . Here  $\rho$  is the fluid density,  $m^*$  the effective mass,  $\gamma/2\pi = -32.435$  MHz/T the gyromagnetic ratio of  $^3\text{He}$ ,  $F_i^s$  the symmetric and  $F_i^a$  the anti-symmetric Fermi-liquid parameters. The temperature-dependent functions  $Z_j$  are defined by

$$Z_j = \pi k_B T \Delta^{j-1} \sum_{n=-\infty}^{\infty} (\epsilon_n^2 + \Delta^2)^{-j/2}, \quad (9)$$

where the Matsubara energies are  $\epsilon_n = \pi T(2n - 1)$  with  $n = 0, \pm 1, \dots, \pm\infty$  and the Yoshida function is given by  $Y = 1 - Z_3(T)$ . In publication [P1] we have measured the field velocity parameter  $\lambda_{\text{HV}}$  as a function of temperature and extracted information on the energy gap  $\Delta(T)$ . The results are discussed in section 4.2.

### 1.3 Nuclear magnetic resonance

The  $^3\text{He}$  atom is a fermion with an odd number of spin 1/2 particles, which allows us to probe the superfluid order parameter using the non-invasive *nuclear magnetic resonance* (NMR) measurement technique. The nuclear magnetic moment of the  $^3\text{He}$  atom in a magnetic field can be excited to resonance at the frequency  $\omega = \gamma H$  by using a small transverse rf field  $\propto e^{i\omega t}$ . The response to small rotations  $\vec{\theta}$  of the spin density  $\vec{S}$  is described by the Leggett equations [8]

$$\frac{\partial \vec{\theta}}{\partial t} = -\gamma \vec{H} + \frac{\gamma^2}{\chi_B} \vec{S}, \quad (10)$$

$$\frac{\partial \vec{S}}{\partial t} = \gamma \vec{S} \times \vec{H} - \frac{\chi_B}{\gamma^2} \Omega_B^2 \hat{n} (\hat{n} \cdot \vec{\theta}), \quad (11)$$

where  $\chi_B(T)$  is the B-phase susceptibility and  $\Omega_B(T)$  the B-phase longitudinal resonance frequency. The transverse resonance response occurs at a frequency which is shifted from the Larmor frequency. In the high-field limit ( $H \gg 2.5\text{mT}$ ) the shift depends on the polar angle  $\beta$  of the unit vector  $\hat{n}$  with respect to the external magnetic field  $\vec{H}$  [9]

$$\omega \approx \sqrt{\omega_L^2 + \Omega_B^2 \sin^2 \beta} \approx \omega_L + \frac{\Omega_B^2}{2\omega_L} \sin^2 \beta, \quad (12)$$

with  $\omega_L = |\gamma|H_L$  the Larmor frequency. The frequency shift is zero when the  $\hat{n}$ -vector is parallel to the magnetic field  $\vec{H}$ . In *continuous wave* (cw) NMR experiments the resonance circuit operates at a fixed frequency  $\nu_{\text{rf}} = \omega_{\text{rf}}/2\pi$  and the NMR absorption  $\chi$  (see section 2.2) is scanned as a function of the externally applied magnetic field  $H$ . The absorption spectra in the magnetic field domain  $H$  can be converted to the frequency domain  $\nu$  using the relation

$$\Delta\nu = \frac{(H_L - H)H}{H_L^2} \nu_{\text{rf}}, \quad (13)$$

where  $H$  is the value of the applied field and  $H_L = \omega_{\text{rf}}/\gamma$  the Larmor field. Using (12) the *reduced* frequency shift  $\tilde{\nu}$  is free from frequency-dependent parameters and is defined as

$$\Delta\tilde{\nu} \equiv \frac{2\omega_L}{\Omega_B^2} (\omega - \omega_L) = \sin^2 \beta. \quad (14)$$

The normalized signal amplitude  $\chi(\omega)$  can be expressed in terms of the dc susceptibility  $\chi_N$  and the measured absorption signal  $V_s$  as

$$\frac{\chi(\omega)}{\chi_N} = \frac{\omega_L \pi}{2} \frac{\chi_B(T)}{\chi_N} \frac{V_s(\omega)}{\int V_s(\omega') d\omega'}, \quad (15)$$

where  $\chi_B(T)/\chi_N$  is defined as the ratio of the total integrated NMR absorptions in the superfluid phase and the normal phase, which can be experimentally determined,

$$\frac{\chi_B(T)}{\chi_N} = \frac{(\int V_s(\omega') d\omega')_T}{(\int V_s(\omega') d\omega')_{T_c}}. \quad (16)$$

The theoretical expression for the static susceptibility using weak-coupling theory is [10]

$$\frac{\chi_B}{\chi_N} = (1 + F_0^a) \frac{\frac{2}{3} + \frac{1}{3}Y(T)}{1 + F_0^a(\frac{2}{3} + \frac{1}{3}Y(T))} \xrightarrow{T \rightarrow 0} \frac{2(1 + F_0^a)}{3 + 2F_0^a}, \quad (17)$$

where  $F_0^a$  is the anti-symmetric Fermi-liquid parameter. The Kramers-Krönig relation tells that the area below the measured *absorption*  $\chi(H)$  signal is a constant, hence one can normalize the spectrum without losing information when only relative signal strength is needed. The spectrum in the frequency domain and *reduced* frequency domain is obtained by dividing out the area between the line shape and the baseline <sup>1</sup>

$$\chi'(\nu) = \frac{\chi(\nu)}{\int \chi(\nu) d\nu}, \quad (18)$$

$$\tilde{\chi}'(\tilde{\nu}) = \frac{\chi(\tilde{\nu})}{\int \chi(\tilde{\nu}) d\tilde{\nu}}. \quad (19)$$

---

<sup>1</sup>Here the symbol  $\chi'$  is used for the normalized absorption signal and not to be confused with the symbol used in literature for the dispersion signal.

The NMR line shape  $\tilde{\chi}'$  is normalized in the reduced frequency domain  $\tilde{\nu}$  and is free of the NMR resonance frequency parameter  $\nu_{\text{rf}}$ .

In numerical calculations we use the *local oscillator model* where the resonance response takes place at the frequency determined by the local value of  $\beta(r)$  [11]. The NMR line shape is then a sum of the individual contributions in the volume  $V$

$$f(\omega) = \frac{1}{V} \int d^3r \delta[\omega - \omega(\vec{r})]. \quad (20)$$

Dephasing of the local oscillators is caused by the inhomogeneity  $\Delta H$  of the polarizing field around the average field value  $H$ . The characteristic dephasing time  $\tau_{\text{H}}$  is of the order of

$$\tau_{\text{H}} = \left( \omega_{\text{rf}} \frac{\Delta H}{H} \right)^{-1} \quad (21)$$

and the delta function in equation (20) becomes a Lorentzian whose width is determined from the NMR line shape in the normal phase or a fitting parameter when the NMR spectrum is compared with numerical calculations.

## 1.4 Vortex lines in $^3\text{He-B}$

The two-fluid model is a phenomenological description of the superfluid [12]. The model treats the superfluid as two interpenetrating fluids: a normal component and a superfluid component. The total fluid density is  $\rho = \rho_{\text{n}} + \rho_{\text{s}}$ , where  $\rho_{\text{n}}$  and  $\rho_{\text{s}}$  are respectively the normal and superfluid density. The total mass current of the superfluid is given by  $\vec{j} = \rho_{\text{n}}\vec{v}_{\text{n}} + \rho_{\text{s}}\vec{v}_{\text{s}}$ . While the superfluid component is inviscid, the normal component behaves as a classical viscous fluid and in equilibrium co-rotates with the container at the velocity  $v_{\text{n}} = \Omega r$ .

The flow velocity in the superfluid  $^3\text{He-B}$  condensate is obtained from the momentum operator  $\hat{p} = -i\hbar\nabla$ . The flow velocity is then expressed as the gradient of the condensates phase

$$\vec{v}_{\text{s}} = \frac{\hbar}{2m_3} \nabla\phi, \quad (22)$$

where  $m_3$  is the mass of the  $^3\text{He}$  atom and the factor 2 originates from the Cooper Pair.

From equation (22) it follows that  $\nabla \times \vec{v}_{\text{s}} = 0$ : the fluid flow is irrotational (or potential). To mimic solid body rotation the superfluid can create an array of rectilinear quantized vortex lines [13, 14]. The circulation  $\kappa$  of a quantized vortex line is obtained by following a closed path  $L$  around the vortex core

$$\oint_L \vec{v}_{\text{s}} \cdot d\vec{l} = \int (\nabla \times \vec{v}_{\text{s}}) \cdot d\vec{S} = n\kappa \quad (23)$$

with  $\kappa = \frac{\hbar}{2m_3} = 0.066 \text{ mm}^2/\text{s}$ . The quantum number  $n = 0, \pm 1, \dots$  gives the lowest energy when  $n = 1$ . Although the order parameter in the vortex core in  $^3\text{He-B}$  does not vanish in the center, as it does in the center of the core of  $^4\text{He}$  vortices, the curl within the  $^3\text{He-B}$  vortex core is non-zero. The B-phase vortex core can be either axisymmetric or non-axisymmetric, which depends on pressure and temperature [15, 16]. At  $p = 29$  bar the transition between

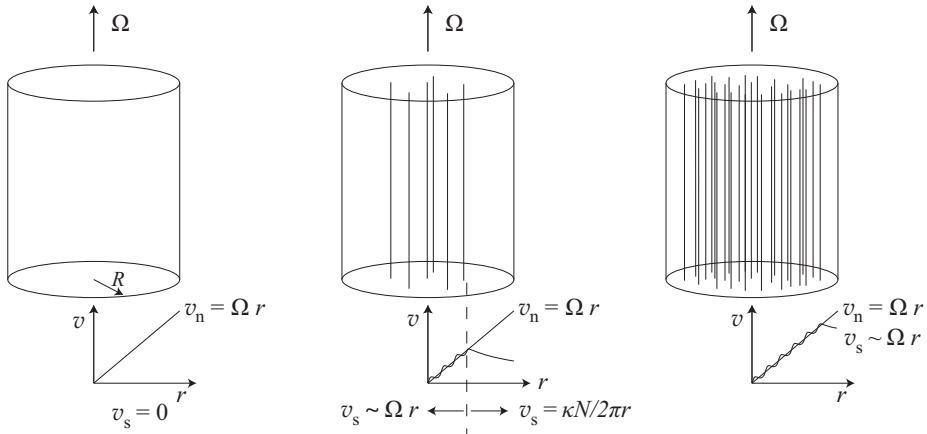


Figure 2: Vortex cluster configurations and corresponding velocity profiles in a rotating cylinder in stationary state conditions. *Left*: vortex free state with the normal component co-rotating with the container, while the superfluid component is at rest. The counterflow  $v_{cf} = v_n - v_s$  is maximal. *Center*: vortex cluster with the number of vortices less than in the equilibrium conditions:  $N < N_v$ . The counterflow inside the cluster is  $v_{cf} \approx 0$ , while outside the cluster  $v_{cf} = \Omega r - \kappa N / (2\pi r)$ . *Right*: the container is filled with the equilibrium number of vortices  $N_v$  and no counterflow is present, except for a small layer (with a width comparable to the inter-vortex distance) adjacent to the surface boundary.

the axisymmetric and non-axisymmetric vortex core occurs at  $0.6 T_c$ . The vortex core radius  $a \sim 10 - 80$  nm is comparable to the superfluid coherence length  $\xi$ .

When superfluid  $^3\text{He}$  is set into rotation, the normal viscous component (with viscosity comparable to olive oil) co-rotates with the container, while the inviscid superfluid condensate stays at rest. See left image in Fig. 2. At the Feynman velocity  $\Omega_{c1} = \frac{\kappa}{2\pi R^2} \ln(R/a)$  the free energy is minimized when a single vortex is at the center of the rotating system. Here  $R$  and  $a$  are respectively the radius of the container and the radius of the vortex core. For a cylinder with  $R = 3$  mm the critical velocity is  $\Omega_{c1} \approx 0.01$  rad/s ( $v_{c1} = 0.03$  mm/s). However, before a vortex nucleates, an energy barrier has to be overcome. For the magnitude of this barrier one compares the energy of a tiny (of vortex core size  $\xi$ ) single vortex loop  $E_{\text{vortex}} \approx \rho_s \kappa^2 \xi$  with the energy of the superfluid flow in the volume of the loop  $E_{\text{flow}} \approx \rho_s v_s^2 \xi^3$ . With  $a \approx \xi$ , the critical velocity where a single vortex nucleates is at the applied flow velocity  $v \approx \kappa/\xi \sim 6$  m/s.

In a rotating cylinder, micron-size particles or defects on the container wall can nucleate a vortex when the flow velocity increases around the sharp corners. Our sample container has been flushed with hydrofluoric acid (HF) to dissolve irregularities on the surface and in places where the quartz has been fused [18]. The now smooth walled container is capable of vortex free flow, up to the critical velocity  $\sim 6$  mm/s. In order to inject a single vortex or a bundle of vortices, different methods can be applied. These are discussed in section 5.2.

A moving vortex in a superfluid mediates the interaction, called mutual friction, between

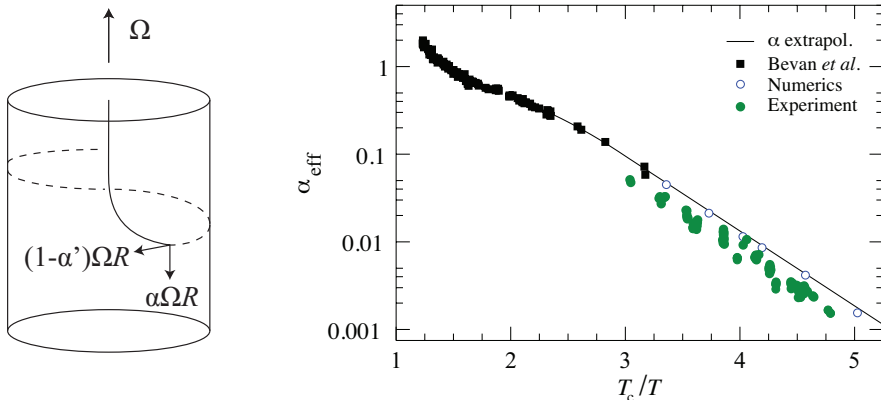


Figure 3: Single vortex motion and the mutual friction parameter  $\alpha$ . *Left*: a single vortex where the vortex end on the surface moves with a spiraling motion around the axis of rotation. The vortex end has the velocity components  $v_\phi = (1 - \alpha')\Omega R$  in the azimuthal direction and  $v_z = \alpha\Omega R$  parallel to the cylindrical axis. *Right*: The mutual friction parameter  $\alpha$  as a function of inverse temperature at  $p = 29$  bar. In the high temperature regime the data of Bevan *et al.* is shown [17]. In the low temperature regime our results are reproduced for the effective mutual friction parameter  $\alpha_{\text{eff}}$  obtained from the relaxation time  $\tau = 1/(2\alpha\Omega)$  of an expanding vortex cluster in spin-down measurements (experiments and numerical simulations) as published in [P2] and [P5]. The spin-down experiments are treated in section 5.3.

the normal and superfluid components. A line segment of a vortex moves in the superfluid with velocity [19]

$$\vec{v}_L = \vec{v}_s + \alpha \hat{s} \times (\vec{v}_n - \vec{v}_s) - \alpha' \hat{s} \times [\hat{s} \times (\vec{v}_n - \vec{v}_s)], \quad (24)$$

with  $\vec{v}_n$  and  $\vec{v}_s$  the local velocities of the normal and superfluid components and  $\hat{s}$  the unit vector along the vortex line segment. The mutual friction parameters  $\alpha$  and  $\alpha'$  are pressure and temperature-dependent [17, 20, 21]. For a single vortex in applied flow, the end of the vortex connected on the cylindrical boundary moves in a spiraling motion with velocity components  $v_\phi = (1 - \alpha')\Omega R$  in the azimuthal direction in the rotating frame and  $v_z = \alpha\Omega R$  parallel to the axis of rotation. Figure 3 shows an illustration of the spiraling vortex motion in applied flow. The figure also shows measured data on the mutual friction parameter  $\alpha$  from spin-down measurements where the relaxation time  $\tau$  of the expanding vortex cluster is related to the mutual friction as  $\tau = 1/(2\alpha\Omega)$ . Spin-down measurements will be treated in section 5.3. Fig. 7 in publication [P7] shows a measurement of a vortex bundle precessing around the cylindrical axis along the surface. The measurement was performed by my predecessor Antti Finne.

In the absence of vortices, i.e. in the vortex-free state, also known as the Landau state, the counterflow velocity is at maximum at a given  $\Omega$ : the normal component is co-rotating with the system, while the superfluid is at rest. This state is metastable. In the laboratory frame the free energy is  $F = E_{\text{kin}} - \Omega I$ , where the extra energy of the vortex free state is

the superfluid kinetic energy  $E_{\text{kin}}$

$$E_{\text{kin}} = 2\pi\rho_s \int_0^R \frac{(\Omega r)^2}{2} r dr = \frac{\pi\rho_s}{4} R^4 \Omega^2 \quad (25)$$

and  $I$  the angular momentum of the rotating superfluid.

When the rotating superfluid system is filled with  $N < N_v$  vortices, where  $N_v$  is the number of vortices in the equilibrium state, the  $N$  vortices form a cluster around the axis of the rotating system with a vortex density corresponding to the applied rotation velocity  $\Omega$ . The counterflow velocity inside the cluster is zero, while outside the cluster  $v_{\text{cf}} = \Omega r - N\kappa/2\pi r$ . In terms of rotation velocity, the counterflow  $\Omega_{\text{cf}} = \Omega - \Omega_v$ , where  $\Omega_v = N\kappa/2\pi R^2$  is the rotation velocity of  $N$  vortices in the equilibrium state. The system is in the equilibrium state when the number of vortices  $N_v$  results in zero counterflow except for a small thin layer at the boundary of width comparable to the inter-vortex distance. Fig. 2 shows the rotating Landau state, a state with  $N < N_v$ , and the superfluid with the equilibrium number of vortices. The corresponding flow profiles are depicted below each picture.

## 1.5 Classical and quantum turbulence

In classical hydrodynamics, the local forces within a compressible classical fluid are described by the Navier-Stokes equation [22]

$$\frac{\partial \vec{v}}{\partial t} + (\vec{v} \cdot \nabla) \vec{v} = \vec{F}/\rho - \nabla p/\rho + \nu \nabla^2 \vec{v}. \quad (26)$$

Here  $\vec{F}$  refers to the external forces per unit volume,  $p$  the pressure, and  $\nu$  the kinematic viscosity. To compare fluids with different kinematic viscosities, the equation is generalized by writing it in dimensionless form. The Navier-Stokes equation is transformed using  $x^0 = x/X$ ,  $v^0 = v/V$  and  $t^0 = Vt/X$ , where  $X$  and  $V$  are the characteristic values for length and velocity. The ratio between the inertial term  $\sim V^2/X$  and the dissipative (viscous) term  $\sim \nu V/X^2$  characterizes the stability of the flow and this is called the Reynolds number  $Re = (V^2/X)/(\nu V/X^2) = VX/\nu$ . When  $Re$  is small, the dissipative term dominates, and the flow is laminar. When  $Re$  is large, the inertial forces are dominant, the flow may become unstable and turbulent [23].

It was Osborn Reynolds in the 18th century who conducted the first systematic series of studies on the stability of classical fluids in pipe flow. He found that at  $Re \approx 2000$ , the fluid became unstable in a burst like manner. Recent experiments have demonstrated that classical fluids can be stable at Reynolds numbers up to  $Re \approx 10^5$  [24]. With increasing Reynolds number  $Re$ , however, the perturbation to trigger turbulence decreases rapidly [25].

In classical turbulence, the fluid motion is irregular: large variations exist in the fluid velocity with eddies on many length scales. The biggest eddies are of size of the system, and carry the largest kinetic energy. While the viscous dissipation is small compared to the energy of these large eddies, kinetic energy is transferred to the smaller eddies. At the smaller length scales viscous dissipation becomes more efficient and removes the kinetic energy from the system. In the energy cascade, the location where the energy is removed from the system is referred to as a sink. In fully developed homogeneous and isotropic turbulence the energy

spectrum is according to the Kolmogorov law  $E \propto \epsilon^{\frac{2}{3}} k^{-\frac{5}{3}}$  [23]. Here  $\epsilon$  is the transfer rate of the energy and  $k$  the wave vector associated with the eddy.

In quantum turbulence, the circulation of superfluid flow is quantized and this simplifies the study of turbulence. The smallest eddy here is a single vortex, while larger eddies are constructed of bundles of several vortex lines. When the flow is locally polarized the mutual friction force per unit volume of superfluid is

$$\vec{F}_{\text{mf}} = -\alpha\rho_s\vec{\omega} \times [\hat{\omega} \times (\vec{v}_n - \vec{v}_s)] - \alpha'\rho_s\hat{\omega} \times (\vec{v}_n - \vec{v}_s), \quad (27)$$

where  $\vec{\omega} = \nabla \times \vec{v}$  is the averaged vorticity and  $\hat{\omega} = \vec{\omega}/\omega$  is the unit vector in the direction of  $\vec{\omega}$ . The mutual friction parameters  $\alpha$  and  $\alpha'$  are discussed in section 1.4. When viscosity of the normal fluid is insignificant and the fluid is incompressible, the Navier-Stokes equation (26) is simplified to the Euler equation. When the mutual friction force  $F_{\text{mf}}$  of equation (27) is the driving force, the coarse-grained hydrodynamic equation becomes

$$\frac{\partial \vec{\omega}_s}{\partial t} = (1 - \alpha')\nabla \times [\vec{v}_s \times \vec{\omega}] + \alpha\nabla[\hat{\omega} \times (\vec{\omega} \times \vec{v}_s)] \quad (28)$$

Following a similar analysis as the Navier-Stokes equation (26), we see that the ratio between the inertial term  $\sim (1 - \alpha')V^2/X$  and the viscous term  $\sim \alpha V^2/X^2$  leads to the superfluid equivalent of the Reynolds number  $Re$ , defined as

$$Re_\alpha = \frac{1 - \alpha'}{\alpha}. \quad (29)$$

At small  $Re_\alpha \ll 1$  the vorticity in the superfluid is over-damped and the fluid flow is laminar, while at  $Re_\alpha \gg 1$ , the vorticity in the superfluid is underdamped and the fluid can become turbulent. Note that the classical Reynolds number depends on the size  $X$  and fluid velocity  $V$ , while in superfluids it is complicated and depends first and foremost on the temperature-dependent mutual friction parameters.

The effective dissipation of a turbulent vortex tangle depends in large part on the interaction between the vortices by reconnections, and thus is a function of the polarization of the vorticity in bundles of vortices. See Fig. 4 for an illustration of a structured and random vortex tangle. In the "structured" tangle the turbulence is of Kolmogorov K41 type and most of the energy is contained in the largest eddy [26]. In the free decay of the vortex tangle, the time dependence of the energy is  $dE/dt \propto t^{-2}$ , which is reflected as a decay in the average vortex line density as  $L(t) = (1.5/\kappa)a\nu^{-\frac{1}{2}}t^{-\frac{3}{2}}$ . Here  $a$  is the size of the largest eddies. The decay of a "random" tangle of vortices is known as Vinen turbulence [27]. Reconnecting vortices create smaller and smaller loops. The time dependence of the energy is  $dE/dt \propto t^{-2}$  with a decay in the average vortex line density according to  $L(t) \propto \nu t^{-1}$ . It is generally assumed that by measuring the decay rate of the vortex line density, the type of turbulence in the experiment can be identified.

In superfluid  $^3\text{He-B}$ , turbulence has been measured by use of a vibrating wire which creates a turbulent vortex tangle at temperatures down to  $0.15 T_c$  [28, 29, 30]. At these temperatures the damping of the vortices by the mutual friction with the normal component is small and has been measured to be temperature independent in the regime  $0.15 \div 0.18 T_c$ . In the rotating state, turbulent bursts have been observed as published in Ref. [31] and in more recent experiments in Refs. [32, 33, 34].

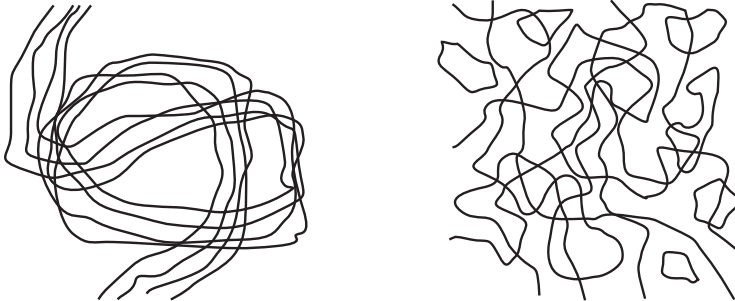


Figure 4: Vortex tangle configurations: *Left*: "Structured" Kolmogorov type turbulence where the eddies are formed by bundles of roughly parallel vortices which can reach in size up to the system size and contain the largest kinetic energy of the system. The vortex line density decreases as  $L(t) \propto t^{-3/2}$ . *Right*: "Random" Vinen turbulence with vorticity at many length scales. Through reconnections of the vortices, the average line density decays as  $L(t) \propto t^{-1}$ . The images are artistic impressions only.

The energy dissipation in quantum turbulence has been measured in spin-down experiments in superfluid  $^4\text{He}$  [35, 36, 37]. Walmsley *et al.* measured the decay in a cubic container filled with superfluid  $^4\text{He}$  and discovered that for the Kolmogorov-type decay with vortex line density  $L(t) \propto t^{-3/2}$  the effective viscosity changes from  $\nu_K = 0.2\kappa$  at high temperatures ( $T > 1$  K) to  $\nu_K = 0.003\kappa$  in the low temperature regime ( $T \ll 1$  K). In the low temperature regime the Vinen-type turbulence with line density  $L(t) \propto t^{-1}$  was determined to have an effective viscosity of  $\nu_V = 0.1\kappa$ .

## 2 Experimental setup

### 2.1 Rotating cryostat

The ROTA cryostat is a low temperature dilution refrigerator combined with a nuclear cooling stage, which holds the experimental container. The cryostat is able to achieve the lowest temperature in rotation. Throughout its history, continuous improvements have been made on this complex machine. What follows is a description of the latest setup starting from the support system down to the heart of the experiment, i.e. the cylindrical quartz container with superfluid  $^3\text{He}$  and the NMR setup. For details on the nuclear stage, NMR magnet, and melting curve thermometer (MCT) we refer to Refs. [43, 44].

Below the floor of the building a large single concrete block provides a solid foundation with a low (eigen) resonance frequency. Four concrete pillars on the block stick through the floor, each holding a single component of an active pneumatic vibration isolation system. See Fig. 5 for a depiction of the setup. A control unit corrects for height displacements by changing the ratio of the flow impedance at the control box with respect to the impedance at the dampers [45]. The pneumatic system was introduced to isolate the frame from vibrations of the pillars, since the resonances of the pillars are weakly coupled to the standing surface waves of the concrete block. Additionally, the four legs are interconnected with demountable crossed steel bars to remove the single pillar resonances. The resonant frequency of the pillars was around 13Hz. On top of the air suspension a frame with four legs supports in the center the axial and radial air bearings of the rotating cryostat.

The cryostat rests on a vertical air bearing (flow rate:  $\frac{\partial}{\partial t}pV = 81 \text{ bar l/min}$ ) and is kept in the center by two radial air bearings (flow rate:  $\frac{\partial}{\partial t}pV = 14 \text{ bar l/min}$  each). In the radial air bearing the spacing for air flow between the cryostat's axis and the fixed support cylinder is  $\sim 30 \mu\text{m}$ . Small size measuring electronics, which runs without mechanical cooling fans, can be placed on a shelf directly on the rotating cryostat. The rotation of the cryostat is provided through a guided adjustable belt system connected to a servo unit with active feedback within the servo. The rotation velocity of the servo is set digitally from the remote computer.

Above the cryostat a separate synchronous carousel is axially aligned with the cryostat. This platform carries the mechanically noisy measurement equipment in order to avoid vibrations entering the refrigerator. The only mechanical connection between this platform and the cryostat are the cables of the measuring instrumentation, power cables and an optical cable for control of the equipment. A high resolution optical encoder with 5000 slits/rev on the axis of the cryostat provides positional information for the second servo control unit, which synchronizes the position of the instrument carousel [46]. The second platform is rotationally aligned within  $1^\circ$  with the cryostat. Between the two platforms a mechanical safety lock ensures that the platforms do not drift too much out of sync.

Carbon slip contacts on the axis of the instrument carousel provide power from an uninterrupted power supply. Optical fiber connections along the axis at the bottom of the dewar and on top of the axis of the instrument carousel allow for data communication between the computer system and the measurement equipment. Another configuration for data communication could have been a wireless network (Wi-Fi), however, the reliability of the setup and the effect of the EMR of the Wi-Fi signal is not known. A Linux based computer system

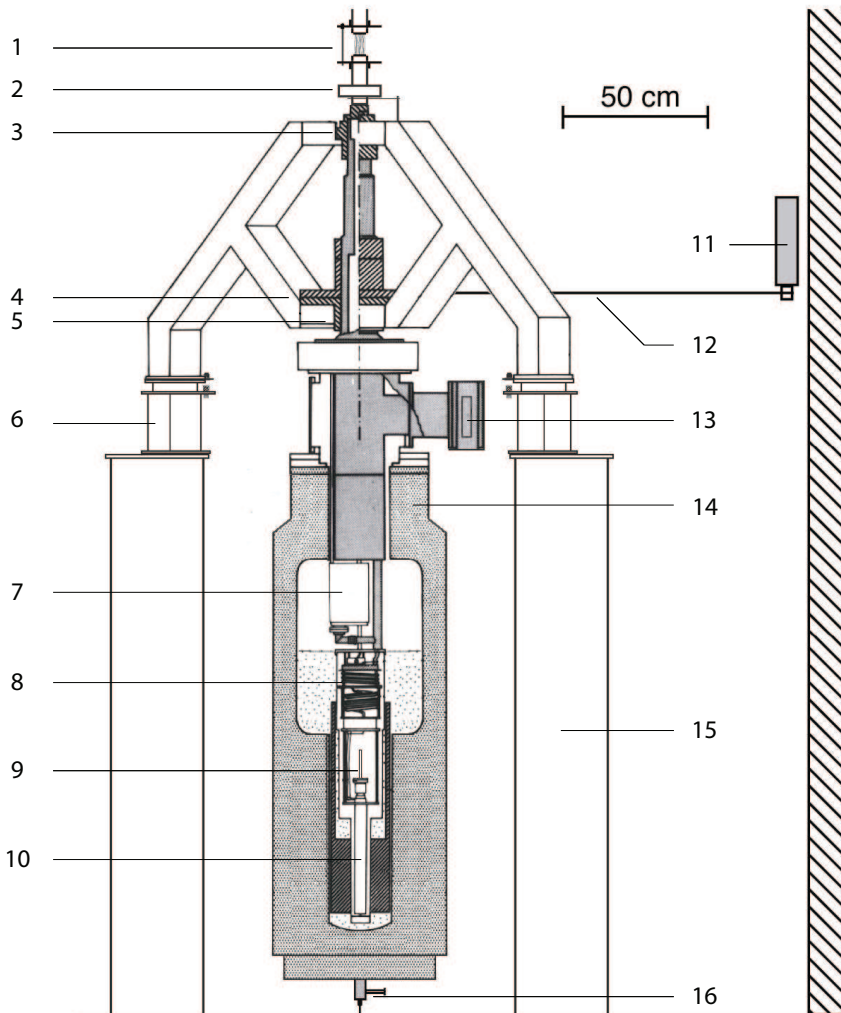


Figure 5: A depiction of the ROTA cryostat. The setup consists of: 1) Safety lock and cables to top rotating platform, 2) Optical encoder, 3) Radial air bearing, 4) Vertical air bearing, 5) Radial air bearing, 6) Vibrational isolator, 7) Cryopump, 8) Dilution refrigerator with sequentially the 1 K-pot, still, heat exchanger and the mixing chamber, 9) Quartz container, 10) Nuclear stage with surrounding superconducting magnet for adiabatic demagnetization cooling, 11) Servo, 12) Flexible belt, 13) Still valve, 14) Dewar, 15) Concrete pillar, 16)  $^4\text{He}$  recovery.

controls the measurement equipment over a TCP/IP, optical fiber, and TCP/IP-to-GPIB network.

The refrigerator assembly includes a liquid helium dewar and a cryostat insert which contains sequentially the 1 K-pot, still, heat exchangers, the mixing chamber and the nuclear cooling stage. The nuclear stage can be thermally decoupled from the mixing chamber with a superconducting heat switch. A vacuum jacket and two radiation shields separate the nuclear cooling stage from the liquid helium bath. The magnet for the nuclear stage is outside the vacuum jacket in the helium bath.

The sample container consists of a quartz glass cylinder filled with superfluid  $^3\text{He}$  at  $p = 29$  bar pressure. Silver powder which is sintered directly on the nuclear stage provides a large surface area and good thermal contact between the fluid and the nuclear stage. A melting curve thermometer (MCT) measures the temperature of the nuclear stage. Adiabatic demagnetization of the nuclear stage enables temperature control. The lowest liquid  $^3\text{He}$  temperature reached is 0.44 mK. The best values for the heat-leak are  $< 2$  nW to the nuclear stage and  $< 12$  pW to the  $^3\text{He}$  sample when the magnetic fields of the NMR are zero.

When the cryostat is not rotating, circulation of  $^3\text{He}$  through the dilution refrigerator is maintained by pumping the evaporated  $^3\text{He}$  from the still with a turbo molecular pump, a roots pump, and rotary pump placed in series. A typical preparation of the cryostat for an experiment proceeds as follows: the copper nuclear coolant is magnetized in a magnetic field of  $H = 7.1$  T. The dilution refrigerator pre-cools the nuclear stage to  $12 \div 14$  mK through the heat switch. The heat switch is aluminum which is a good heat conductor when it is maintained in the normal state with a magnetic field. Pre-cooling of the nuclear stage and the  $^3\text{He}$  liquid takes 2-4 days. After opening the heat switch, a slow demagnetization ( $\sim 4$  hours) of the nuclear stage lowers the temperature of the stage to  $\sim 2$  mK at a magnetic field value of 0.9 T. The demagnetization process is close to adiabatic. It takes  $\sim 6$  hours for the liquid in the cell to be in thermal equilibrium with the nuclear stage at  $T_c$ .

To enable rotation of the cryostat, the circulation is stopped by closing and disconnecting the condensing line, the 1 K-pot line, and the still line. In the *single cycle mode*, the evaporated  $^3\text{He}$  is absorbed by a cryopump located around the still outlet. The cryopump houses active charcoal fixed on copper substrates which are cooled to  $\sim 6$  K by a flow of  $^4\text{He}$  gas which is evaporated from the dewar bath by a heater. The  $^4\text{He}$  gas from the bath is recovered through an axially mounted rotating joint at the bottom of the dewar. The mixing chamber holds enough  $^3\text{He}$  to sustain the single cycle mode for up to 30 hours.

## 2.2 Nuclear magnetic resonance setup

In this section we discuss the two sample setups from *2005* and *2009*. The main differences between the setups are the geometry of the pickup coils, the NMR signal detection and the setup of the quartz tuning forks. The mechanical properties of the forks are discussed in section 3.

In our cw-NMR setup we make use of a LC-resonator circuit in a Q-meter-like circuit where the changes in the susceptibility of the  $^3\text{He}$  fluid are measured by comparing the voltage across the inductance  $L$  in the presence of  $^3\text{He}$  liquid to an unloaded inductance  $L_0$  of the coil,

$$L = L_0(1 + \zeta\chi(\omega)), \quad (30)$$

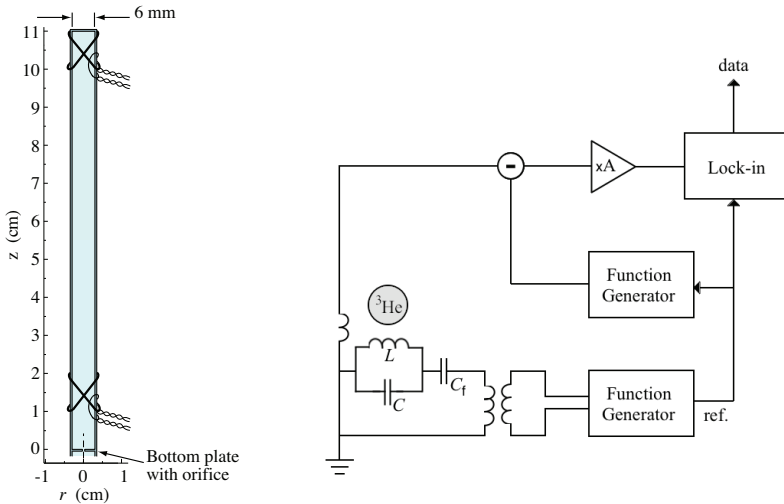


Figure 6: Experimental setup from 2005: the left figure shows the experimental quartz cylinder with a detector coil at both ends of the NMR sample volume. The right figure shows schematically the LC-resonance circuit in a Q-meter setup. The superfluid is excited with a high-Q LC-resonator and changes in the coil inductance are measured. The signal is compensated by a second phase locked function generator for high resolution measurement. The differential signal is recorded with the Stanford Research Systems SR560 differential amplifier. A phase lock-in amplifier (Stanford Research Systems model SR844) is used for data acquisition.

where  $\chi(\omega) = \chi_d(\omega) - i\chi_a(\omega)$  is the dynamic susceptibility and  $\zeta$  the filling factor. The absorption  $\chi_a$  and dispersion  $\chi_d$  components are measured simultaneously. The filling factor is a measure of the volume of the  $^3\text{He}$  affected by the resonance coil. At fixed resonance frequency, the magnetic field is swept and  $\chi$  changes. The quality factor  $Q$  of the oscillator is defined as

$$Q = \omega \frac{\text{stored energy}}{\text{dissipated power}}. \quad (31)$$

Using superconducting materials in the circuit resistive losses are reduced. The dielectric losses in special high-Q capacitors are insignificant [47]. In the setups described below, the detector coils are made of thin ( $50 \mu\text{m}$ ) Nb/Ti superconducting wire in a Cu/Ni matrix.

The *2005 setup* had above the sintered silver heat-exchanger two quartz tuning forks below the  $^3\text{He}$  NMR sample volume. The main volume of the long quartz cylindrical container with superfluid  $^3\text{He}$  was in thermal contact with the fork volume through a tiny orifice ( $\text{Ø} = 0.75 \text{ mm}$ ) in the bottom plate, see Fig. 6. This division plate prevents vortices from entering the main volume from the volume with the forks.

Two NMR detector coils are placed close to the ends of the cylindrical container. The pickup loop close to the NMR coil provides loose coupling of the measurement equipment

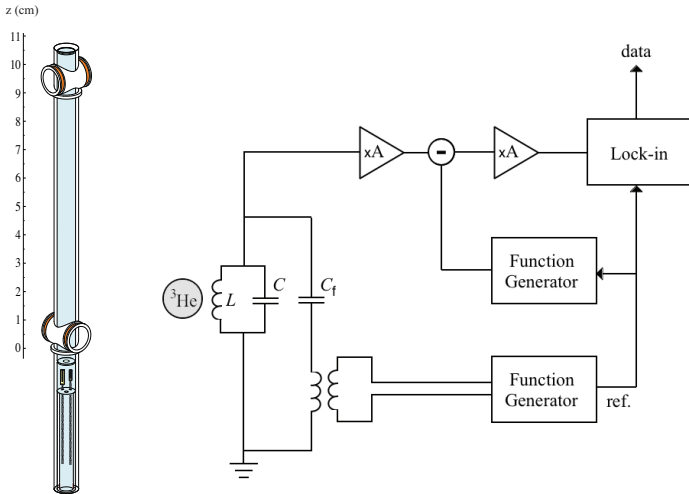


Figure 7: Experimental setup in 2009: the left figure shows the experimental quartz cylinder with the  $^3\text{He}$  superfluid. Below the main volume, two quartz tuning forks are located in an isolated volume which separates the sinter volume from the main volume. The temperature within the fork volume is dominated by the quasiparticle flux from the main volume. At both ends of the main volume, two detector coils measure the superfluid  $^3\text{He}$  response. After amplification at low temperatures, the signal is compensated with a second function generator in the Stanford Research Systems SR560 differential amplifier. Data acquisition is established by a phase lock-in amplifier (Stanford Research System model SR844)

to the tank circuit. The compensation signal from a second function generator is phase locked to the resonance circuit function generator and the combined signal is amplified at room temperature with a Stanford Research System SR560 differential amplifier. A lock-in amplifier (Stanford Research Systems model SR844) is used for data acquisition. The resonance circuit was tuned to  $\nu_{\text{rf}} = 965.0 \text{ kHz}$  which corresponds to a Larmor field of  $H_L = 29.75 \text{ mT}$  in the superfluid  $^3\text{He}$ . The tank circuit has a quality factor of  $Q = 6050$ . The field inhomogeneity was measured a number of times (after different cool downs to liquid helium temperatures) in the Fermi-liquid state with low enough excitation not to saturate the signal. The NMR line shape was distorted and far from ideal Lorentzian. The determination of field inhomogeneity by fitting the superfluid NMR line shape with calculations gave consistently  $\Delta H/H \approx 8.8 \cdot 10^{-4}$  at all measured temperatures.

The *2009 setup* had above the sinter two quartz tuning forks in an isolated volume separated with a second orifice ( $\text{Ø} = 0.3 \text{ mm}$ ) from the sinter volume, see Fig. 7. Since the upper orifice is much larger, the quasiparticle flux from the main volume dominates the quasiparticle density in the fork volume. In effect, the temperature measured by the forks reflects the temperature of the superfluid in the main volume. This fork setup allows for measurements of the thermal signal from the dissipation produced by the propagating vortex front when it replaces vortex-free counterflow with the equilibrium vortex state. The fork

together with the orifice forms a bolometer and is able to measure thermal fluctuations on the order of 0.1 pW in the background heat leak [48].

The main sample volume is a cylindrical container with a NMR resonator coil at each end. The NMR coil geometry is not of Helmholtz type, where the separation  $d$  between the coils is equal to the radius of the coils. Compared to the *2005 setup*, the coils here had a smaller packing factor, i.e. the volume of the sample sensitive to the NMR oscillating field, but had a  $3 \div 5$  times better signal-to-noise ratio due to the addition of a cold pre-amplifier: the resonance circuit has a pre-amp at 4 K and a second amplifier at room temperature [49]. The resonance frequency of the circuit is  $\nu_{\text{rf}} = 1.967$  MHz, which corresponds to a Larmor field of  $H_{\text{L}} = 60.65$  mT. The measured field inhomogeneity in the NMR response was  $\Delta H/H = 8.3 \cdot 10^{-4}$ . The circuit had a quality factor of  $Q = 3900$ . The transverse rf field of the spectrometer coil was  $H_{\text{rf}} = 3.4$  nT and the coil had an inductance of  $L = 12.7 \mu\text{H}$  [49]. The NMR magnet produces magnetic fields up to at least  $H = 61$  mT for measurement with Larmor resonance frequencies at  $\nu_{\text{rf}} = 2$  MHz. The typical sweep rate of the NMR field is  $\dot{H} = 9 \div 13 \mu\text{T/s}$ . In the spectra analysis, the magnetic field value  $H$  is obtained by measuring the current through the coil. The actual field value lags behind owing to the  $L/R$  time constant of the sweep magnet. In the spectrum analysis a small linear correction is applied to the field value  $H$ , such that the NMR line shapes (absorption as a function of magnetic field) in up and down sweeps of the magnet overlap.

### 3 Quartz tuning forks in superfluid $^3\text{He}$

Mechanical oscillators submerged in a superfluid are useful tools to study the hydrodynamic properties of quantum fluids. It was the torsional oscillations experiments by Andronikashvili [50, 51, 52] (using a stack of closely spaced discs) that observed the normal ( $\rho_n$ ) and superfluid ( $\rho_s$ ) components in He II. In more recent studies, alternative types of oscillators have been used: i) spheres [53, 54], grids [55, 56], and wires [57] in  $^4\text{He}$ ; ii) grids [58], and wires [59] in  $^3\text{He}$ ; iii) wires [60] in  $^3\text{He}$ - $^4\text{He}$  mixtures. In superfluid  $^3\text{He}$ , vibrating wires are typically used to measure the viscosity as a function of temperature or dissipative effects by attached vortex lines. A vibrating wire consists of a thin superconducting wire, either straight or looped, in a static magnetic field, where the drive originates from the Lorentz force induced by the oscillating current through the wire. Operating at relatively low frequencies (on the order of 1 kHz), these wires have to be very thin to become sensitive at the very lowest temperatures. Recently, factory machined quartz tuning forks were proposed as a new type of mechanical oscillator in superfluids. Forks are piezoelectric resonators, which are cheap, robust, and easy to install. For the use in electronic watches, the forks are frequency tuned to  $32.768 \pm 0.06$  kHz. It was hoped that this property would give reproducible results between different forks when used in superfluids, but this appeared not to be the case.

In this chapter we describe our collaborative research of quartz tuning fork, which resulted in publications [P8] and [P9]. We describe the mechanical properties of the fork in vacuum and when submerged in a (super)fluid. The response of the fork in  $^3\text{He}$  is discussed in the linear regime in the normal and superfluid state. The measurements are compared with results of vibrating wire experiments. As an illustration of the sensitivity of the forks, an example of a bolometric measurement is given: the fork's response shows an image of the NMR line shape due to changes in the quasiparticle density when the NMR line shape of the superfluid  $^3\text{He}$ -B is scanned at ultra low temperatures. We discuss a set of experiments in which forks driven at high velocities are used as a generator of quasiparticles and vortex tangles. We conclude with a demonstration of Andreev reflection: the screening effect of quasiparticles by vortex tangles as measured by a detector fork at low velocity.

#### 3.1 Mechanical properties and hydrodynamics

The mechanical properties of the fork are discussed in vacuum and the model is "dressed up" by including mass enhancement effects due to the oscillating fluid close to the surface of the fork. When the fork is driven at sufficiently small amplitudes using a harmonic force  $F = F_0 \cos(\omega t)$ , the drag force is linear in the velocity dependence. The equation of motion of the prong is

$$\frac{d^2x}{dt^2} + \gamma \frac{dx}{dt} + \frac{k}{m}x = \frac{F}{m}. \quad (32)$$

Here the parameters are the effective mass  $m$ , drag coefficient  $\gamma$ , the spring constant  $k$  and the driving force  $F$ . The equation has the harmonic solution  $x(t) = x_a(\omega) \sin(\omega t) + x_d(\omega) \cos(\omega t)$ , where  $x_a$  and  $x_d$  are the absorption and dispersion, respectively. At resonance  $\omega_0 = \sqrt{k/m}$ , the mean absorbed power  $\langle F dx/dt \rangle = F_0 \omega_a/2$  is at maximum (where  $F_0$  is the amplitude of

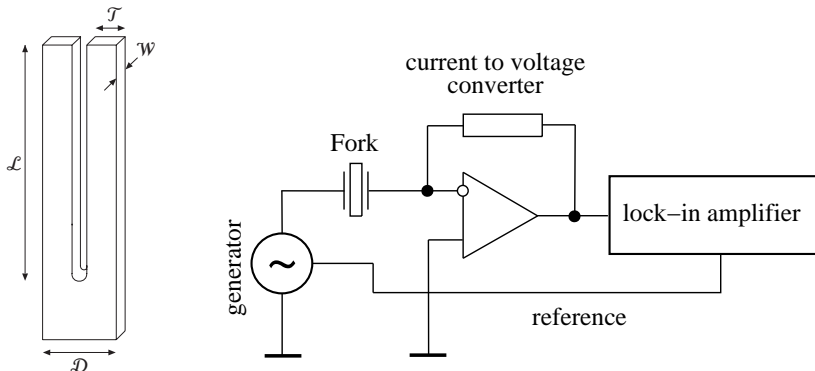


Figure 8: Quartz tuning fork geometry and electrical circuit diagram: *Left*: In the 2005 setup we used forks with  $\mathcal{L} = 3.12$  mm,  $\mathcal{W} = 0.352$  mm,  $\mathcal{T} = 0.402$  mm, and  $\mathcal{D} = 1.0$  mm. After replacing the magnetic leads on the fork with superconducting wire, the measured resonance frequency was  $f_0 = 36293$  Hz. The quality factor  $Q$  of the fork at room temperature in vacuum was  $Q = f_0/\Delta f \approx 2.7 \cdot 10^4$ . *Right*: An attenuated function generator drives the fork. The deflection of the fork generates a current (piezo-electric effect), which is measured – after conversion to voltage – with a lock-in amplifier.

the harmonic force). The quality factor of the fork is defined as

$$Q = \frac{\omega_0}{\Delta\omega}, \quad (33)$$

with  $\Delta\omega = \gamma$  the full width of the resonance curve at half of the maximum power.

Applying an oscillating voltage  $U = U_0 \cos(\omega t)$  on the electrodes at the base of the fork, the piezoelectric effect excites the prongs. The stress of the deflection induces a current proportional to the derivative of the deflection

$$I(t) = a \frac{dx(t)}{dt}. \quad (34)$$

The parameter  $a$  can be calibrated by comparing equation (32) with the corresponding differential equation for the current

$$\frac{d^2 I}{dt^2} + \frac{R}{L} \frac{dI}{dt} + \frac{I}{LC} = \frac{1}{L} \frac{dU}{dt} \quad (35)$$

and equalizing  $\omega_0^2 = 1/(LC)$ ,  $\gamma = R/L$ , and using equation (34),  $1/L = (F_0/U_0)a/m$ . The correspondence is completed when the electrical driving power  $U_0^2/(2R)$  is equal to the dissipated power  $2 \cdot F_0^2/(2m\gamma)$  of the two prongs. The connection becomes

$$F_0 = (a/2)U_0, \quad (36)$$

$$R = 2m\gamma/a^2, \quad (37)$$

$$L = 2m/a^2, \quad (38)$$

$$C = a^2/(2k). \quad (39)$$

From equation (37) parameter  $a$  can be determined by using  $\gamma = \Delta\omega$ , the width of the fork resonance curve, and the  $1/R$  dependence from the linear slope in the experimental  $I_0(U_0)$  dependence. Here the nought (zero) refers to the fork at resonance. The resonance curves in vacuum are

$$I_a = \frac{a^2 U_0}{2} \frac{m\gamma\omega^2}{(m\gamma\omega)^2 + (m\omega^2 - k)^2} = \frac{I_0(\Delta\omega)^2\omega^2}{(\Delta\omega)^2\omega^2 + (\omega^2 - \omega_0^2)^2} \quad (40)$$

$$I_d = \frac{a^2 U_0}{2} \frac{\omega(m\omega^2 - k)}{(m\gamma\omega)^2 + (m\omega^2 - k)^2} = \frac{I_0\Delta\omega\omega(\omega^2 - \omega_0^2)}{(\Delta\omega)^2\omega^2 + (\omega^2 - \omega_0^2)^2} \quad (41)$$

The fork submerged in a viscous fluid experiences drag from the boundary layer. The depth of the penetration into the fluid is

$$\delta = \sqrt{\frac{2\nu}{\omega}} = \sqrt{\frac{2\eta}{\rho\omega}}, \quad (42)$$

where  $\omega$  is the angular frequency of the oscillation, while  $\eta$  and  $\nu = \eta/\rho$  are the dynamic and kinematic viscosities of the fluid with density  $\rho$ . The back flow effectively enhances the mass of the prongs compared to the prongs in vacuum. The additional force leads to a reduction of the resonance frequency  $\omega$ , while the resonance curve increases in the width  $\gamma$ :

$$\omega_0^2 = \omega_{0\text{vac}}^2 (m_{\text{vac}}/m), \quad (43)$$

$$\gamma = \gamma_{\text{vac}}(m_{\text{vac}}/m) + b/m. \quad (44)$$

Here  $b$  characterizes the potential flow field around the fork, which depend on the geometry, the viscosity  $\eta$  and the applied frequency  $\omega$ .

### 3.2 Tuning fork response in the linear regime

Since the drag on the prongs is a function of the temperature-dependent viscosity of the fluid, the fork can be used as a secondary thermometer. The left panel in Fig. 9 shows the forkwidth  $\Delta f$  as a function of temperature, calibrated against a melting curve thermometer. Above the superfluid transition temperature  $T_c$  the viscosity of normal  $^3\text{He}$  varies as  $\eta \propto T^{-2}$  and the forkwidth follows the  $1/T$  behaviour from Fermi-liquid theory, see right panel Fig. 9. Vibrating wires show close to  $T_c$  the so-called viscous anomaly, i.e. deviation from viscous response [62], while the forks do not.

Cooling  $^3\text{He}$  through  $T_c$ , the fork response expressed in  $\Delta f$  decreases rapidly when entering the superfluid A-phase and a discontinuity is observed at the AB-phase transition at  $T_{\text{AB}}$ . Further cooling in the B-phase shows a continuous decrease in  $\Delta f$ , primarily caused by the rapid decline of the normal component  $\rho_n$ . Below  $0.3T_c$  the  $^3\text{He}$ -B superfluid is in the ballistic regime and the dependence can be extrapolated using  $Q = f_0/\Delta f \propto \exp(\Delta/k_B T)$ , where  $\Delta(T, p)$  is the superfluid energy gap. The proportionality factor in this calibration can be fixed at one known temperature. To summarize the calibration scheme: down to  $0.3T_c$  the fork is calibrated against the MCT, while in the ballistic regime, the forkwidth follows the exponential dependence on the quasiparticle density.

In the ballistic regime, minute changes in the fluid temperature can be observed in the fork response  $\Delta f$ . As an illustration of this sensitivity, we show the fork response  $\Delta f$  when

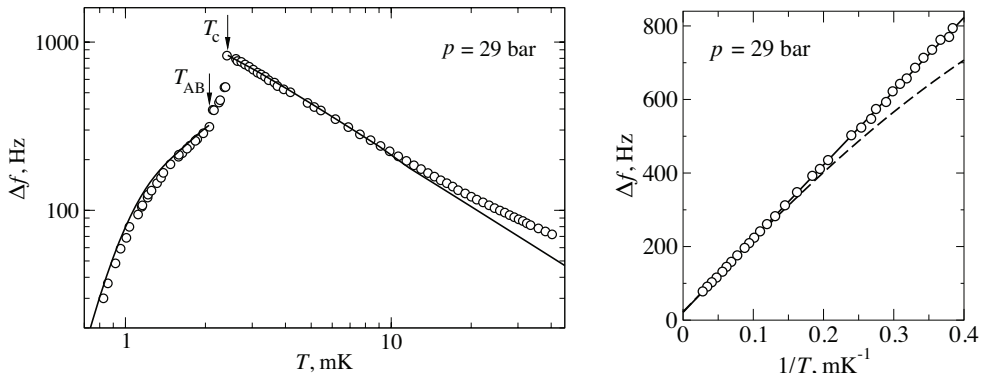


Figure 9: Resonance width of the quartz tuning fork in  $^3\text{He-B}$  at 29 bar pressure. *Left panel:* Measured (circles) forkwidth  $\Delta f$  as a function of temperature  $T$ . The width of the fork is strongly reduced when cooled through  $T_c$  where the behaviour changes from Fermi-liquid to superfluid. The solid line is the predicted behaviour of a vibrating wire resonator with the same density  $\rho$  and resonant frequency  $f_{0\text{vac}}$  [61]. The thickness of the wire is fixed to 0.25 mm, which is comparable to the dimensions of the fork's prong. *Right panel:* Measured resonance width of the fork (circles) above  $T_c$  as a function of inverse temperature  $1/T$ . The solid line is a linear fit of  $\Delta f$  versus  $1/T$ . The dashed curve shows the effect from a viscosity anomaly close to  $T_c$  as measured with a vibrating wire in [62]. The viscous anomaly is not observed in the measurements of the fork.

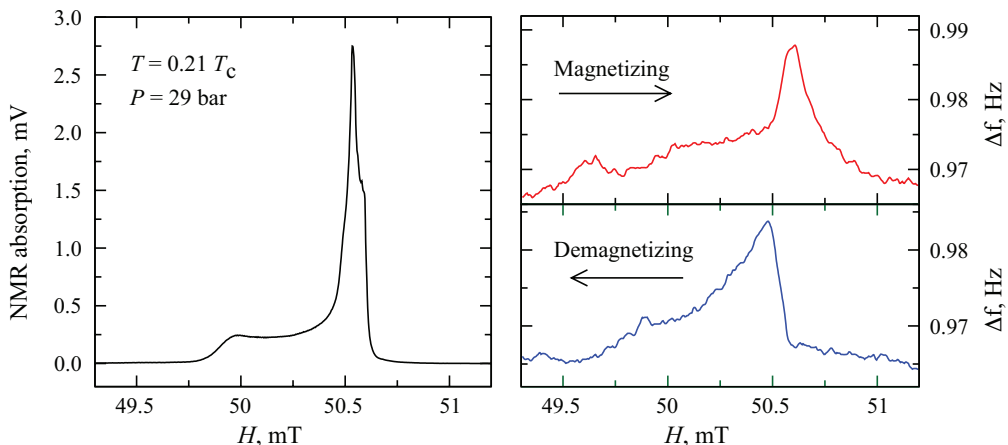


Figure 10: Bolometric measurement of the NMR absorption using a quartz tuning fork. *Left panel:* The NMR absorption spectrum at zero rotation velocity is measured as a function of the magnetic field. *Right panel:* The absorption  $I_a$  of the fork is recorded during the sweep of the magnetic field of the NMR. The reconstructed fork response  $\Delta f$  is shown for an upward (top figure) and downward (bottom figure) sweep of the NMR field intensity. Differences between the line shapes are caused by the finite relaxation time of the bolometer.

the NMR spectrum of the simple flare out texture is measured. In this exercise the fork is at resonance  $\omega_0$ , while the NMR absorption and dispersion signals were recorded. The current in the NMR magnet was swept up/down, to record the entire NMR spectrum. The different absorption levels during the NMR sweep change the quasiparticle density which is detected by the fork. When the NMR scan has been completed, the response in the fork width can be reconstructed from its absorption and dispersion signals as a function of time. After the NMR scan, the full spectrum of the fork resonance spectrum is measured and used as a reference in the conversion of the forks absorption signal to  $\Delta f$ . Here we make use of the relation  $\Delta f \cdot I_a = \text{constant}$ , where  $I_a$  is the absorption of the fork at resonance. Fig. 10 shows both the NMR absorption and the fork response during an upward/downward sweep of the NMR field intensity. Differences in the fork response during the up- and downward sweep of the NMR are due to relaxation after a significant absorption of heat, in particular at the Larmor field  $H = 50.6$  mT.

### 3.3 Andreev reflection from a vortex tangle

At low excitations, the response of the fork's velocity  $\dot{x}$  to the driving force  $F$  is linear, i.e.  $\dot{x} \propto F$ . In the low temperature regime, the motion of the fork prongs are damped by the scattering of quasiparticle excitations in the superfluid. The damping force per unit area is [63]

$$F_T = p_F \langle nV_g \rangle \left[ 1 - \exp\left(\frac{-\lambda p_F}{k_B T} \dot{x}\right) \right], \quad (45)$$

where  $V_g$  is the group velocity of the excitations,  $p_F$  the Fermi momentum,  $\dot{x}$  the velocity of the prong,  $\lambda$  a constant characterizing the velocity field around the object, and  $\langle nV_g \rangle = n(p_F)k_B T \exp(-\Delta/k_B T)$  represents the quasiparticle flux. Here  $n(p_F)$  is the density of states in momentum space. When  $p_F \dot{x} \ll k_B T$ , the first three terms of the Taylor expansion yield

$$F_T = n(p_F)p_F^2 \lambda \exp(-\Delta/k_B T) \left[ 1 - \frac{\lambda p_F}{2k_B T} \dot{x} \right] \dot{x}. \quad (46)$$

The first term is the velocity-independent damping coefficient  $\gamma$  which is responsible for the linear damping force  $F_T^{\text{lin}} = \gamma \dot{x}$ . The second term is the velocity-dependent term  $\beta(\dot{x}) = \gamma \lambda p_F \dot{x} / 2k_B T$  is the contribution from Andreev reflection to damping. The total damping coefficient  $\gamma - \beta(\dot{x})$  relates to the linewidth  $\Delta f$ , hence the contribution of Andreev reflection can be measured. Fig. 3 in publication [P9] shows the measured linewidth  $\Delta f$  as a function of velocity  $\dot{x}$ . Initially  $\Delta f$  is constant, but decreases with increasing velocity  $\dot{x} \propto F$ . Here quasiparticles are screened by the vortex tangle around the fork. The exchange of the momenta of the scattered quasiparticles is of the order of  $(\Delta/E_F)p_F$ , where  $E_F$  is the Fermi energy. At sufficiently large drive,  $\Delta f$  starts to increase again. The velocity where this occurs is the pair breaking velocity  $\sim 1$  mm/s (in the right panel), above which the fork's motion produces pair breaking and/or generates turbulence, similar to the case of vibrating wire experiments [59, 63].

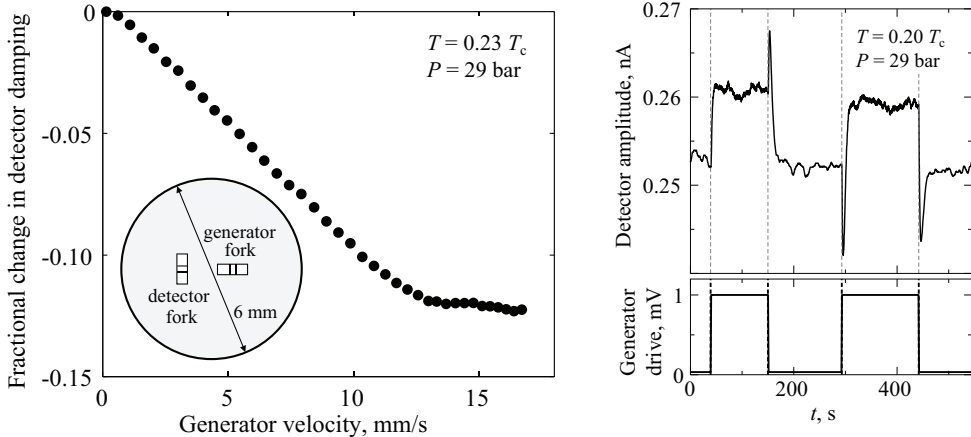


Figure 11: Andreev reflection on a vortex tangle: *Left panel*: The relative change in (corrected) forkwidth of the detector fork plotted as a function of the drive velocity of the generator fork. With increasing drive the generator fork creates a tangle which partially surrounds the detector fork. Quasiparticle reflection on the vortex tangle (Andreev reflection), reduces the damping on the detector fork. The inset shows the positions of the two forks in the quartz tube. The temperature of the fluid is  $T = 0.23 T_c$ , i.e. it is in the ballistic regime. *Right panel*: Andreev reflection: reflection of the resonance amplitude of the detector fork to a pulsating drive of the generator fork. During a pulse, the generator fork creates a vortex tangle, which shields the detector fork from quasiparticles. The damping is reduced and the resonance amplitude increases.

A more illustrative example of Andreev reflection is the experiment with two forks, where one fork acts as a generator and the other as a detector. The two forks are located in the bottom section of the quartz sample tube in the setup of 2005, as shown in Fig. 6. The forks partially block the 6 mm diameter quartz tube, which connects to the sintered heat exchanger. The end of the quartz tube is  $\sim 2$  mm from the sintered heat exchanger. When the generator fork is excited at high drive, the heat flux  $\dot{Q}$  causes a temperature rise which is registered by the detector fork. Heat carried by the quasiparticles flows along the tube toward the heat exchanger. The thermal resistance  $R_T = \Delta T / \dot{Q} = R_0 (k_B T / \Delta) \exp(\Delta / k_B T)$  is dominated by the area  $A_h$  of the restriction. In the blackbody radiator model for quasiparticle flux, the thermal resistance is defined as  $R_0 = 2\pi^2 \hbar^3 / (p_F^2 \Delta k_B A_h)$  [64]. In our measurements we have determined the area of the constriction as  $A_h = 3 \text{ mm}^2$ . For the procedure of this measurement, see Fig. 4 in publication [P9]. The forks experience a temperature increase which is reflected by the increase in  $\Delta f$ .

The left panel of Fig. 11 shows the relative change of the forkwidth of the detector, i.e. corrected for the temperature increase, as  $(\Delta f - \Delta f_0) / \Delta f_0$ , where  $\Delta f$  is the measured response of the fork and  $\Delta f_0(T)$  is the temperature-dependent width in the absence of screening. The right panel shows the recorded response of the detector fork where the drive of the generator fork is pulsed. The detector fork is driven at low velocity (below 0.5 mm/s),

while the square pulses of the generator are at relatively high velocity (5.6 mm/s). Although the generator fork increases the temperature of the fluid, the measured response in the detector fork is an apparent cooling. This phenomenon represents Andreev reflection of quasiparticles from the vortex tangle created by the generator fork, which partially surrounds the detector fork. The screening lowers the quasiparticle density around the detector, which is reflected by a decrease in its fork width  $\Delta f$ .

## 4 Textural energies and NMR spectra

In this section we discuss the results published in [P1] on the flare out texture of the order parameter and the comparison of the measured NMR line shape with numerical calculations. The detailed analysis was critical for the interpretation of the counterflow spectra and for determining the number of vortex lines, which was needed in publications [P2,P4-P6].

### 4.1 Flare out textures of $^3\text{He-B}$ in applied flow

The order parameter texture of superfluid  $^3\text{He-B}$  in a cylindrical container with an applied magnetic field  $H$  parallel to the cylindrical axis is axially symmetric. Without a magnetic field an in-plane texture is also possible [66], but we concentrate on the axially symmetric case. Thus ideal flare-out textures in the absence of textural defects have two important properties: they are (1) axially symmetric and (2) they can be represented with a continuous function. A priori, the orientation of the  $\hat{n}$ -vector at the center and at the cylindrical wall is already known: the  $\hat{n}$ -vector in the center (i.e.  $r = 0$ ) is parallel to  $\vec{H}$ , hence  $\beta = 0$ . Additionally, the Cooper Pair angular momentum density  $\vec{L}$  close to the surface must be perpendicular to the boundary, otherwise mass flow would be through the surface. With  $\theta = \arccos(-1/4)$ , the condition for the angle  $\beta$  becomes  $\sin^2 \beta(R) = 0.8$  (i.e.  $\beta \approx 63.4^\circ$ ). Thus in the flare out textures the  $n$ -axis orientation changes smoothly from the center of the container from  $\beta(0) = 0^\circ$  towards the container surface with  $\beta \approx 63.4^\circ$ .

When the flow is applied by rotating the container, the superfluid component stays in rest, while the normal component co-rotates with the container. The orbital anisotropy axis  $\hat{l}$  wants to align in the direction of the counterflow ( $\vec{v}_n - \vec{v}_n$ ), which couples the orientation of the density anisotropy  $\delta\rho^{(n)} = \rho_\perp^{(n)} - \rho_\parallel^{(n)}$ . This enhances the anisotropy energy  $F_{\text{HV}}$  (8). Finally the gradient energy  $F_G$  (5) smoothens out the local variations and produces the smoothly varying distribution of  $\hat{n}$  orientations. The result is the so-called *simple flare out* texture in Fig. 12, as expressed in terms of the azimuthal angle  $\alpha$  and polar angle  $\beta$  in the inset. The *simple flare out* texture does not change as a function of the rotation velocity up to  $\Omega_{t1} \gtrsim 0.2 \text{ rad/s}^2$ .

Sufficiently large flow finally tilts  $\hat{n}$  enough, such that in a region where the applied flow is largest, the angle  $\beta$  becomes nearly constant. This region is at large radii close to the cylindrical surface. In NMR absorption experiments this results in the first appearance of the cf-peak at the critical rotation velocity  $\Omega_{t1}$ . This texture is the *parted flare out* texture. Fig. 13 shows in the bottom part a measurement and the corresponding NMR spectrum of the calculated texture. Increasing the applied flow further, results in an extension of the region of nearly constant polar angle  $\beta$  and a correspondingly larger counterflow peak height.

An abrupt transition occurs at the critical rotation velocity  $\Omega_{t2}$  where the angle  $\beta$  now has flipped over at the surface boundary. In the spectrum the texture change results in the widening of the spectrum, and a shift of the cf-peak. The smoothly varying texture with  $\beta(0) = 0^\circ$  to  $\beta(R) \approx 116^\circ$  crosses in the vicinity of the cylindrical surface the  $90^\circ$  angle. This texture is known as the *extended flare out* texture. Here in a region close to the surface

---

<sup>2</sup>In our publication [P1] the critical rotation velocity is expressed as  $\Omega_{c1}$ , but this notation is here already reserved for the Feynman critical velocity for the creation of a single vortex.

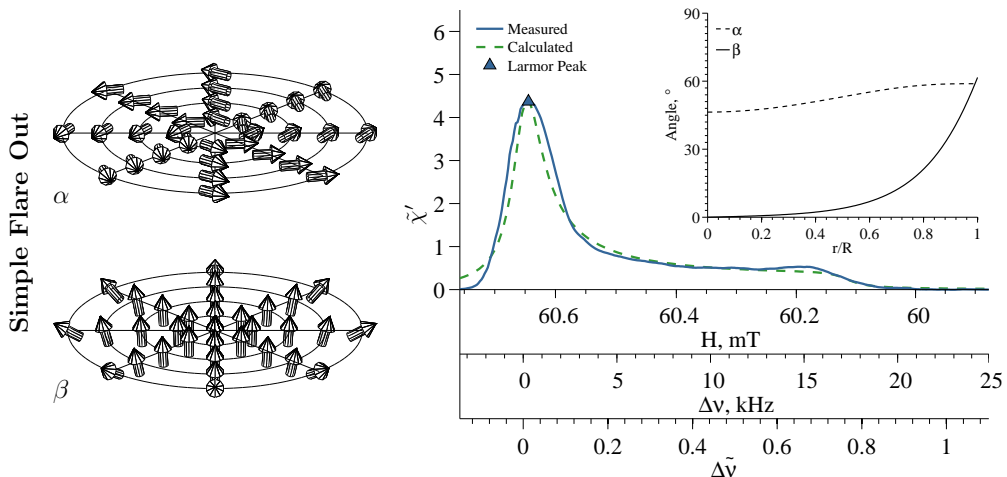


Figure 12: The simple flare out texture. The measured and calculated NMR line shapes of the *simple* flare out textures of  $^3\text{He-B}$  in a cylindrical cell with radius  $R = 3$  mm. The measured spectra are presented as a function of the magnetic field  $H$ , or equivalently the frequency shift  $\Delta\nu = \nu - \nu_L$  from the Larmor frequency  $\nu_L$ , or as a reduced frequency shift  $\Delta\tilde{\nu} = \sin^2 \beta$ . On the vertical scale the signal amplitude is the normalized dynamic susceptibility  $\chi'$  from (19). The associated textures, i.e.  $\hat{n}$ -vector representation (by means of the angles  $\alpha$  and  $\beta$ ) as a function of reduced radius are depicted in the inset and on the left. Parameters of the *simple* flare out texture: fork temperature  $T = 0.251 T_c$ , pressure  $p = 29$  bar, rotation velocity  $\Omega = 0.2$  rad/s with no vortices, cw-NMR frequency  $\nu_{\text{rf}} = 1.967$  MHz and Larmor field  $H_L = 60.65$  mT.

boundary where the counterflow is the largest, the angle  $\beta$  again is constant. Increasing the applied flow results in a larger region of constant  $\beta$ . The top graph in Fig. 13 shows a measurement of this texture and the corresponding fitted calculation.

The critical velocities  $\Omega_{t1}$  and  $\Omega_{t2}$  depend on the fluid's pressure, temperature, and the applied magnetic field, as well as the radius  $R$  of the container. Fig. 14 shows our results a cylindrical container with radius  $R = 3$  mm measured at a liquid pressure of 29 bar. A comparison is made with the data of Korhonen *et al.* [38]. The critical velocity  $\Omega_{t1}$  in our measurements is roughly constant down to  $\sim 0.4 T_c$ , but increases rapidly with decreasing temperature below  $0.4 T_c$ . The transition  $\Omega_{t1}$  is a 2nd-order phase transition and does not show hysteresis within the precision of the used velocity step  $\Delta\Omega = 0.025$  rad/s. The rapid increase of  $\Omega_{t1}$  with decreasing temperatures shows that NMR experiments become more and more problematic, if the analysis is based on the variations in the counterflow peak height: the cf-peak simply vanishes even at high rotation velocities. However, our measurements show that at  $0.2 T_c$ , the contribution of the counterflow to the absorption spectrum is still appreciable if the applied flow is above  $\sim 0.9$  rad/s.

The critical transition at  $\Omega_{t2}$  shows similar behaviour: below  $0.4 T_c$  the transition velocity increases rapidly. Large hysteresis is seen as a function of the applied velocity and

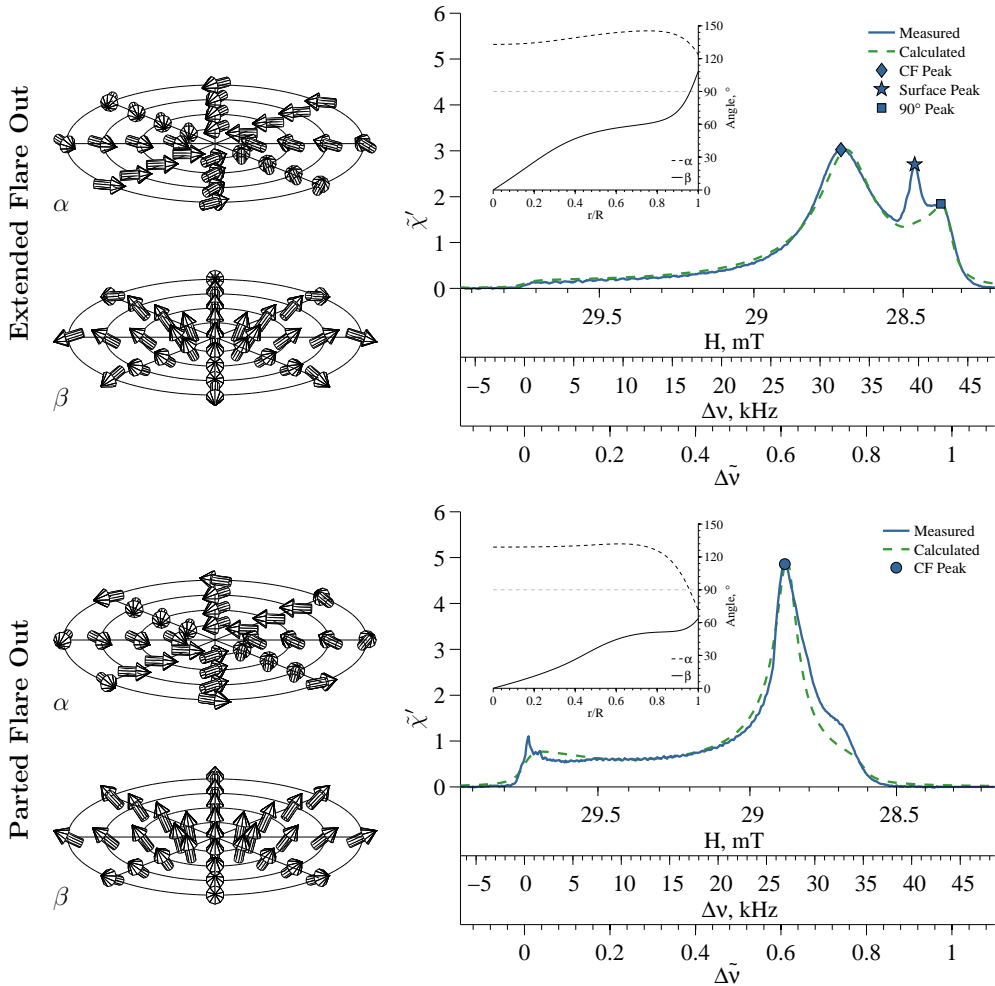


Figure 13: Order parameter textures and NMR spectra in applied flow. The measured and calculated NMR line shapes of the *parted* and *extended* flare out textures are compared for a cylindrical sample of 3 mm radius. The associated textures, i.e.  $\hat{n}$ -vector representation (by means of the angles  $\alpha$  and  $\beta$ ) as a function of reduced radius are depicted in the inset and on the left. Parameters of the *parted flare out* texture: fork temperature  $T = 0.313 T_c$ , pressure  $p = 29$  bar, rotation velocity  $\Omega = 0.9$  rad/s with vortex cluster  $\Omega_v = 0.1$  rad/s, cw-NMR frequency  $\nu_{rf} = 965.0$  kHz and Larmor field  $H_L = 29.75$  mT; *extended flare out* texture:  $T = 0.359 T_c$ ,  $\Omega = 0.7$  rad/s with no vortices,  $\nu_{rf} = 965.0$  kHz and  $H_L = 29.75$  mT. In the calculations the temperature was treated as a fitting parameter since it controls the frequency shifts via the Leggett frequency  $\Omega_B(T)$ . Other fitting parameters; *parted* flare out texture: field velocity parameter  $\lambda_{HV} = 3.14$  kg/m<sup>3</sup>T<sup>2</sup> and field inhomogeneity  $\Delta H/H = 8.79 \cdot 10^{-4}$ ; *extended* flare out texture:  $\lambda_{HV} = 5.85$  kg/m<sup>3</sup>T<sup>2</sup> and  $\Delta H/H = 8.79 \cdot 10^{-4}$ .

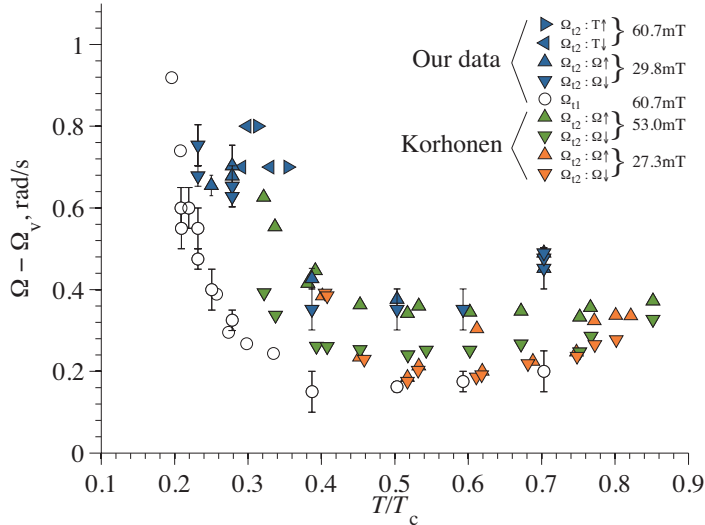


Figure 14: Textural phase transitions: the figure shows the critical velocity  $\Omega_{t1}$  (between *simple* and *parted* flare out textures) and  $\Omega_{t2}$  (between *parted* and *extended* flare out textures) given as the cf velocity  $\Omega_{cf} = \Omega - \Omega_v$  versus reduced temperature. The first critical velocity  $\Omega_{t1}$  is constant down to  $0.4T_c$  and then increases rapidly. The second critical velocity  $\Omega_{t2}$  was measured in *setup 2005* at constant rotation velocity by sweeping the temperature ( $T \uparrow$ : increasing temperature), and in the *setup 2009* at constant temperature by varying rotation velocity ( $\Omega \uparrow$ : rotation is increased in steps  $\Delta\Omega$ ). The pressure of the  $^3\text{He}$  liquid was  $p = 29$  bar. Our results are compared with data of Korhonen *et al.* (1990) at  $p = 10.3$  bar pressure [38]. Larmor field values are given in the legend.

temperature. In the *parted* flare out texture, the transition velocity grows rapidly larger with decreasing temperature such that below  $0.3T_c$  the velocity needed for the transition was not achieved up to the critical velocity  $\Omega_{cr}$  where vortices spontaneously form.

The critical textural transition between the *parted* and *extended* flare out textures at  $\Omega_{t2}$  shows hysteresis both in temperature and in the applied velocity. For an illustration of these phenomena, see Fig. 5 and Fig. 6 in publication [P1].

## 4.2 Counterflow and density anisotropy

The counterflow between the normal and superfluid components is maximal when the rotating superfluid is vortex free. When vortices enter the system, the counterflow is reduced and this is reflected as a decrease in the counterflow peak height. Since the pickup coils surround the whole cross section of a part of the cylindrical container only the global counterflow can be measured. In publication [P1] we studied the height and the frequency shift of the counterflow peak as a function of temperature, as well as a function of the number of vortices.

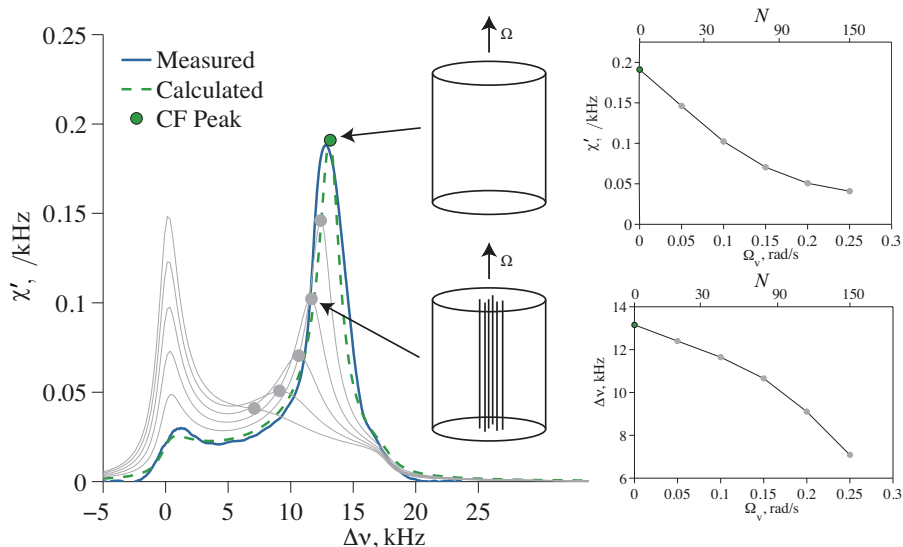


Figure 15: NMR absorption spectra as function of the size of the central vortex cluster: The left figure shows the experimental (thick solid) and the optimal calculated (dashed) line shape of vortex free flow at  $0.232 T_c$  rotating at  $\Omega = 0.9$  rad/s. The NMR resonance frequency was at  $\nu_{\text{rf}} = 1.97$  MHz. The optimal value for the field velocity parameter was  $\lambda_{\text{HV}} = 0.94$  kg/m<sup>3</sup>T<sup>2</sup>. The thick solid line represents a measured spectrum for vortex-free counterflow to which the calculations have been fitted (dashed line shape). The gray curves show the calculated line shapes with an increasing number of vortices; the differences between the adjacent lines shapes is  $\Delta\Omega_v = 0.05$  rad/s. With increasing number of vortices, the counterflow peak decreases. The top right panel shows the absorption at the counterflow peak as a function of the vortex number  $N$  and the corresponding value of  $\Omega_v$ . The bottom right figure shows the frequency shift of the counterflow peak as a function of  $N$  and  $\Omega_v$ .

Earlier systematic measurements were performed down to  $\sim 0.45 T_c$  and we extended this range down to  $0.2 T_c$  [6, 9]. Fig. 15 shows the measured and calculated NMR line shapes in rotation with varying number of vortices in the *parted* flare out texture. At low vortex numbers, the counterflow peak height reduces rapidly, while at a large number of vortices the cf-peak becomes less sensitive. The cf-peak vanishes completely when the transition velocity  $\Omega_{\text{t1}} = \Omega - \Omega_v$  is reached. This condition is valid when the number of vortices expressed as  $\Omega_v$  is small compared to the drive  $\Omega$ . With increasing number of vortices the frequency shift decreases until close to Larmor frequency where the cf-peak disappears. The graphs on the right in Fig. 15 show the cf-peak height and frequency shift as a function of the applied flow and number of vortices.

The integrated absorption in the spectra is a function of the rf excitation applied to the NMR coil, the amplification of the detector, and the static susceptibility  $\chi_B/\chi_N$  of the <sup>3</sup>He fluid. Hence, it is preferred to perform the analysis of the cf-peak height dependence

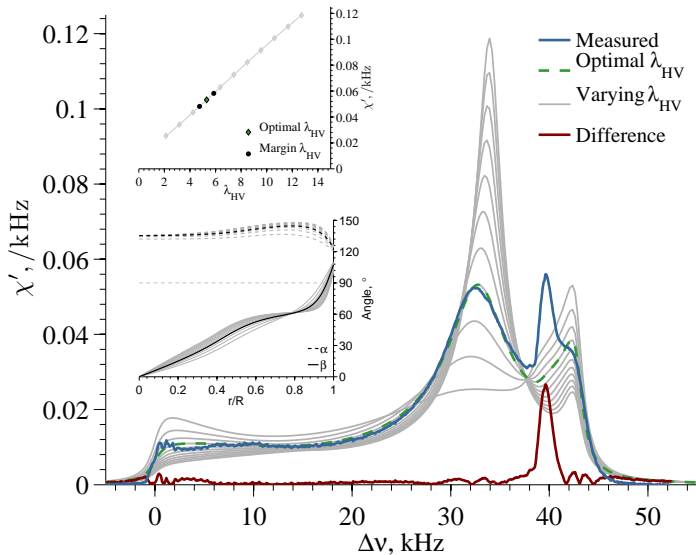


Figure 16: Fitting procedure for the field velocity parameter  $\lambda_{\text{HV}}$ : the main panel shows the measured spectrum (blue) of the superfluid at  $0.34 T_c$  rotating at  $0.9 \text{ rad/s}$  with a vortex cluster of  $\Omega_v = 0.1 \text{ rad/s}$ . The calculated spectrum (dashed green) is shown for the optimal value  $\lambda_{\text{HV}} = 5.3 \text{ kg/m}^3 \text{T}^2$ . The different line shapes drawn with gray curves are calculated by varying  $\lambda_{\text{HV}}$  around the optimal value (the bottom inset shows the corresponding  $\hat{n}$ -vector textures). This gives the dependence of the cf peak on  $\lambda_{\text{HV}}$ , which is used for estimating the uncertainty in  $\lambda_{\text{HV}}$ . Taking the absolute difference between the measured spectrum (blue) and the calculated spectrum (dashed green) isolates the *surface peak* (red). Note that the area under the surface peak is the main contributor to the uncertainty in  $\lambda_{\text{HV}}$  as it directly influences the normalization of the measured spectrum.

on the number of vortices in the normalized spectrum. In the normalized spectrum, the counterflow peak height depends on the alignment of the orbital anisotropy axis  $\hat{l}$  with the global flow, and reflects the change in density anisotropy  $\delta\rho_{\parallel}^{(n)} - \rho_{\perp}^{(n)}$  expressed through the parameter  $\lambda_{\text{HV}}$ . By comparing the experimentally obtained spectra to the calculated spectra, the density anisotropy parameter  $\lambda_{\text{HV}}$  can be determined.

Fig. 16 shows a line shape measurement of the order parameter texture in a cylindrical cell with radius  $R = 3 \text{ mm}$ . The optimal value for the parameter  $\lambda_{\text{HV}}$  was found when the cf-peak height and frequency shift agreed with those of the calculated NMR line shape. Since the field inhomogeneity also influences the absorption at the cf-peak, the solution for  $\lambda_{\text{HV}}$  is not uniquely determined. However, a unique solution can be found when  $\lambda_{\text{HV}}$  is extracted using both the *parted* and the *extended* flare out texture measured at the same applied flow and temperature. Additionally,  $\lambda_{\text{HV}}$  can also be extracted from the first appearance of the cf-peak in the *parted* flare out textures, but with loss of precision. The uncertainty in the optimal value of  $\lambda_{\text{HV}}$  was determined by relating the uncertainty in the area under the

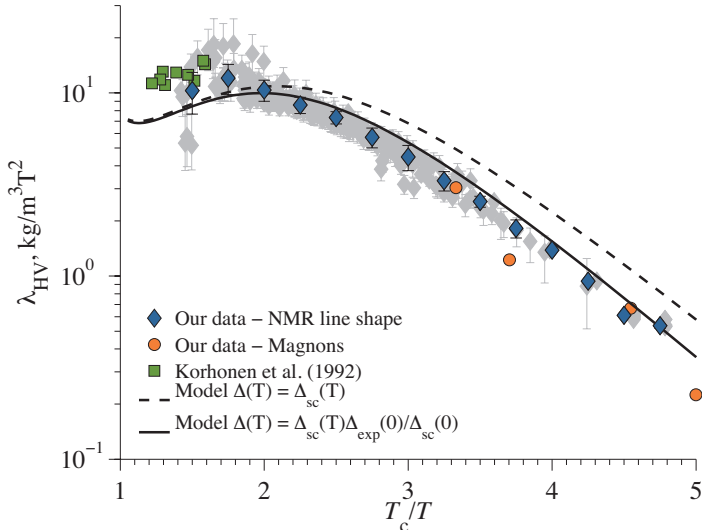


Figure 17: Field velocity parameter  $\lambda_{\text{HV}}$  as a function of inverse temperature. Our data using NMR line shape measurements (gray markers, 350 individual NMR spectra),  $\lambda_{\text{HV}}$  was obtained using the fitting procedure as described in Fig. 16. Blue markers show averages within the inverse-temperature bins; on these markers the error-bars indicate  $\pm 1$  standard deviation. In the low temperature regime, data is shown where  $\lambda_{\text{HV}}$  is obtained from fitting  $\lambda_{\text{HV}}$  in experiments with magnons in the potential well [67]. In the high temperature regime data is shown from Korhonen *et al.* [42]. Dashed and solid lines represent the model of the field velocity parameter  $\lambda_{\text{HV}}$  (8) with the energy gaps  $\Delta_{\text{sc}}$  and  $\Delta_{\text{scaled}}$ , respectively.

measured absorption line shape to the cf-peak height in a linear manner. From the upper and lower boundaries of the cf-peak height, the corresponding upper and lower boundaries of  $\lambda_{\text{HV}}$  were determined, see top inset of Fig. 16. The bottom inset shows the  $\hat{n}$ -vector orientations in the calculated order parameter textures, as expressed in terms of the angles  $\alpha$  and  $\beta$ . In general, the counterflow peak depends strongly on  $\lambda_{\text{HV}}$  in the measured temperature range where  $\lambda_{\text{HV}}$  itself changes almost two orders of magnitude.

The difference between the measured and calculated NMR line shapes in Fig. 16 reveals an absorption peak in the measured spectrum. The peak is only present in the *extended* flare out texture below  $\sim 0.45 T_c$  and is never observed in the *parted* or *simple* flare out texture. In publication [P1] we have concluded that this absorption relates to a spin-wave resonance in the potential well near the surface boundary as earlier suggested by Salomaa [39]. Fig. 12 in publication [P1] shows its reduced frequency shift as a function of temperature and the inset shows the corresponding potential well,  $U \propto \sin^2 \beta$ , from the calculated order parameter texture. The frequency shift of the peak with decreasing temperature corresponds qualitatively with the change in the potential well.

Measurements on the parameter  $\lambda_{\text{HV}}$  using the procedure as depicted in Fig. 16 have

been performed with a variety of vortex cluster sizes ( $\Omega_v = 0, 0.1, 0.25$  rad/s) and rotation velocities ( $\Omega = 0.4 \div 2$  rad/s). Fig. 17 shows the resulting parameter  $\lambda_{\text{HV}}$  as a function of temperature. The two curves show the predictions from theory using different values for the energy gap  $\Delta(T)$ , see equation (8). From the measurements below  $T \sim 0.3 T_c$  the data show better agreement with the scaled energy gap,  $\Delta_{\text{scaled}}$ , than with the *strong-coupling* corrected energy gap from weak-coupling theory,  $\Delta_{\text{sc}}$ . The corrected gap is also known as *wc<sup>+</sup>* (weak-coupling plus). From the measurements by Davis *et al.* [40], the extrapolated value for the gap at  $p = 29$  bar in the low temperature limit corresponds to  $\Delta_{\text{sc}}(0) = 1.87 k_B T_c$ . The gap we use is the scaled energy gap,  $\Delta_{\text{scaled}} = \Delta_{\text{exp}}(0) \Delta_{\text{sc}}(T) / \Delta_{\text{sc}}(0)$ , where we use linear scaling of the strong-coupling corrected energy gap,  $\Delta_{\text{sc}}(T)$ , such that in the low temperature limit the energy gap corresponds to  $\Delta_{\text{exp}}(0) = 1.97 k_B T_c$ , as measured by Todoshchenko *et al.* [41]. The temperature measurement of the data in Fig. 17 was determined from the calibrated forkwidth  $\Delta f$  against the MCT and extrapolated in the ballistic regime  $T < 0.3 T_c$  using the dependence of the width on the quasiparticle density:  $\Delta f \propto \exp(-\Delta/k_B T)$ . In the above described comparison between theoretical curves with different gap values, we rescaled the temperature axis for both energy gaps such that the appropriate energy gap was used consistently. For the temperature axis in Fig. 17 we have used the gap  $\Delta_{\text{exp}}(0) = 1.97 k_B T_c$ . A rescaling of the temperature axis with  $\Delta_{\text{sc}}(0) = 1.87 k_B T_c$  moves the points below  $0.25 T_c$  to slightly lower values, but not significantly. Better agreement with the theoretical curve of  $\lambda_{\text{HV}}$  is obtained with  $\Delta_{\text{exp}}(0) = 1.97 k_B T_c$ .

## 5 Vortex dynamics in superfluid $^3\text{He-B}$

### 5.1 Preparing the Landau state in rotation

In the temperature range  $0.7T_c \leq T < T_{\text{AB}}$  the dynamics of superfluid  $^3\text{He-B}$  at  $p = 29$  bar is overdamped, since the superfluid Reynolds number (29)  $Re_\alpha \ll 1$ . Here  $T_{\text{AB}}$  is the AB-phase transition, see Fig. 1. In this regime when the rotation velocity  $\Omega$  is increased from rest to a final rotation velocity  $\Omega_f$  (spin-up experiment) no vortices are created in the process if the final rotation velocity does not exceed the critical velocity  $\Omega_{\text{cr}}$ . The normal component co-rotates at  $\Omega_f$  with the cylinder, while the superfluid is at rest. This is the meta-stable Landau state in rotation with the kinetic energy  $E_{\text{kin}} = \pi\rho_s\Omega_f^2 R^4/4$ . Probing the superfluid order parameter with NMR reveals a large counterflow peak in the spectra. If the system contains a small number of vortices, these would expand along the cylinder and their number would remain constant. The vortices would form a cluster in the center of the cylinder. For a numerical calculation of the reorganization of remanent vortices, see Fig. 2 in publication [P4]. From this point on, the vortex free state, or the state with a small cluster of vortices, can be cooled down to a temperature of at least  $0.2T_c$  without the creation of additional vortices. This procedure has been crucial in the study of vortex injection experiments as described in section 5.4.

### 5.2 Vortex formation in applied flow

The vortex number is not necessarily conserved in applied flow experiments if the superfluid Reynolds number  $Re_\alpha \gg 1$ . Earlier measurements by A. Finne *et al.* had showed a transition to turbulence when the rotating Landau state was perturbed by injecting a bundle of closely spaced small vortex loops [44]. In those experiments, the bundle of loops was released from the AB interface using the Kelvin-Helmholtz instability of the AB-phase boundary. After injection, the number of vortices in the B-phase increases rapidly in a sudden short burst of turbulence. This phase transition in the vortex dynamics marks the onset to the temperature regime where bulk turbulence becomes possible. The transition temperature is  $T_{\text{on}}^{\text{Bulk}} \approx 0.59T_c$  at  $p = 29$  bar pressure. See Fig. 4 of [P5] and Ref. [33] for a phase diagram. The onset to turbulence was also observed in experiments where the rotating superfluid in the Landau state was irradiated with thermal neutrons. Close to the cylindrical surface the neutron undergoes the capture reaction:  $n + {}^3_2\text{He} \rightarrow p + {}^3_1\text{H} + 764\text{keV}$ . The localized heating from this exothermic reaction leads to vortex formation via the Kibble-Zurek mechanism [70, 71, 72, 73]. These vortices are introduced in the form of small rings in the counterflow. At temperatures below the onset to turbulence they may interact to produce a sudden turbulent burst of vortex formation.

In this section we describe the process which leads to turbulence in spin-up experiments: the instability of expanding vortices with respect to loop formation and reconnections at the cylindrical wall. We conclude this section with the unexpected observation of laminar vortex flow in the bulk volume in the zero temperature limit. The laminar bulk region is surrounded by a thin surface layer which coats the cylindrical wall. Within this surface layer the new vortices are continuously created in surface reconnections.

*Remanent vortices in applied flow:* The evolution of a low number density vortices at

zero rotation velocity has been studied by increasing the rotation velocity of the container, and thereby subjecting the remnants to the applied flow. As a result the remnants start expanding in order to become rectilinear vortex lines. Typically their both ends are connected to the cylindrical surface, where these end points describe a helical trajectory during the spirally expanding motion. At high temperatures these expanding remnants are stable in the sense that their number is conserved. A profound change is observed when the superfluid Reynolds number becomes sufficiently large at low temperatures,  $Re_\alpha \gg 1$ , below some case dependent onset temperature  $T_{\text{on}}^{\text{wall}}$ . Below this onset temperature, the expanding vortices reconnect at the cylindrical wall and produce new independently moving small loops. These loops similarly start expanding, but when sufficiently many loops manage to interact a localized burst may take place. As an illustration, a numerical simulation of a vortex ring colliding with a solid surface is depicted in Fig.9 of publication [P5]. When a turbulent burst is observed, enough vortices have been generated to form the equilibrium vortex state. We have performed measurements of the onset temperature  $T_{\text{on}}^{\text{wall}}$  using different numbers of remanent vortices and concluded that the transition temperature  $T_{\text{on}}^{\text{wall}}$  depends on the initial number of remnants, their configuration, and the applied counterflow velocity. Although the process is stochastic in nature, the onset temperature is rather sharp. An illustration of the transition is depicted in Fig.3 of publication [P4].

*Equilibrium vortex state in elevated rotation:* A rotating tilted cylinder with a vortex cluster in the equilibrium state usually includes some outermost vortices which are not rectilinear but connect at one end to the cylindrical surface. These so-called seed vortices where one of vortex ends connects to the curved surface and the other end connects to the end plate of the cylinder. The number of seed vortices depends on the size of the cluster through the rotation velocity  $\Omega_v$ , the length of the cylinder, as well as the tilt of the cylinder (in our experiments  $\sim 1^\circ$ ). See Fig.4 in publication [P4]. When the flow is increased, the seed vortices expand along the cylindrical axis with a spiraling motion on the surface around the axis. The seed vortices become unstable when their motion is underdamped at  $Re_\alpha > 1$ . At this onset temperature  $T_{\text{on}}^{\text{wall}}$ , the vortex number initially increases slowly with a rate of  $\dot{N} = 0.3 \div 2.5$  vortices/s and is then followed by a burst of turbulence. At the moment of the burst, the rate at which the number of vortices increases is beyond our measurement capability (maximum resolved rate:  $\dot{N} \sim 5$  vortices/s). For examples of a vortex multiplication measurement, see Fig.6 and Fig.7 in publication [P4]. The time for the burst to occur depends on the applied flow  $\Omega_{\text{cf}} \sim \Delta\Omega$  through the step change in rotation velocity  $\Delta\Omega$ , as well on the temperature: the burst occurs earlier with increasing flow, as well with decreasing temperature, see Fig.11 [P4]. With increasing number of seed vortices or larger applied flow  $\Omega_{\text{cf}}$ , the transition temperature  $T_{\text{on}}^{\text{wall}}$  increases. For an illustration of the dependence on the number of seed vortices, see Fig.18. The figure shows the probability distribution as a function of temperature at which the system becomes turbulent. We compare measurements with different number of seed vortices, while the applied flow is kept the same.

*Vortex generation in  $T \rightarrow 0$  limit:* The dynamics of superfluid  $^3\text{He-B}$  under rotation in the limit  $T \rightarrow 0$ , where  $Re_\alpha \rightarrow 1/\alpha \gg 1$ , was expected to become turbulent at any condition. The reasoning was that the damping of vortices at  $T < 0.3T_c$  decreases rapidly since the quasiparticle density decreases exponentially with decreasing temperature in the ballistic regime. Measurements in superfluid  $^4\text{He}$  have been shown to be turbulent in both spin-up

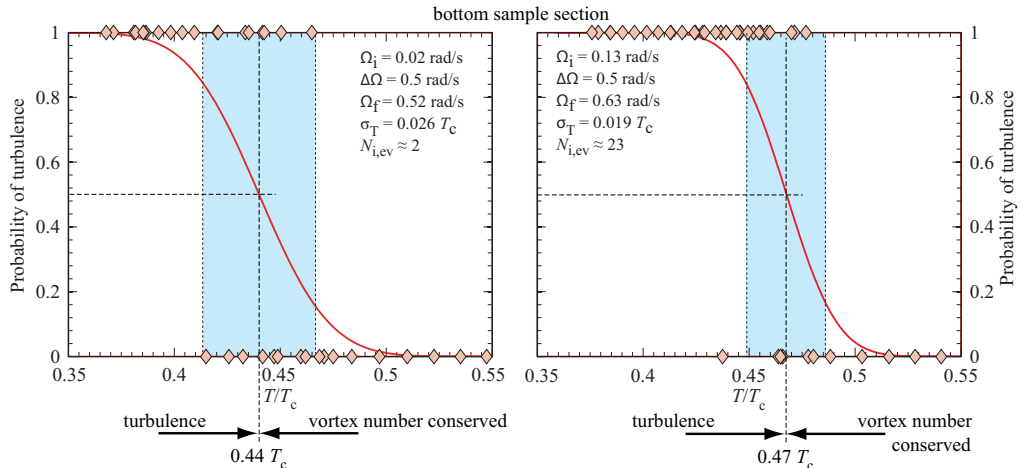


Figure 18: Onset temperature measurements with a varying number of seed vortices. A comparison is made of the onset temperature to turbulence of two cases of equilibrium vortex states with a different number of seed vortices while the applied flow is identical. In these experiments the superfluid state was prepared with the equilibrium number of vortices of which some vortices (seeds) connect to the cylindrical surface. The rotation velocity is increased by  $\Delta\Omega = 0.5 \text{ rad/s}$  and the transient process and the final state are observed. When the final state has counterflow, no turbulent process occurred, and the final state is marked with a zero. If the transient process was turbulent, the final state of the superfluid shows no counterflow peak in the NMR spectrum and the state is marked as "1". From these measurements, the onset temperature with a Gaussian width are determined. *Left panel:* Rotation step up from  $\Omega_i = 0.02 \text{ rad/s}$  with approximately 2 seed vortices. *Right panel:* Rotation step up from  $\Omega_i = 0.13 \text{ rad/s}$  with approximately 23 seed vortices. From these two figures it is concluded that the onset temperature to turbulence  $T_{\text{on}}^{\text{wall}}$  increases when the number of seed vortices increases.

and spin-down experiments: see Ref. [68] for measurements in a cylinder and Ref. [36] for a cubical geometry. The cause of turbulence in  $^4\text{He}$  is the creation of a turbulent Ekman boundary layer close to the surface owing to strong surface pinning. However, in our experiments in superfluid  $^3\text{He-B}$ , vortices are continuously created at the surface boundary after which the vortices move in a laminar fashion towards the center to form a cluster! This discovery resulted in publication [P2]. The main difference with superfluid  $^4\text{He}$  is the much larger vortex core radius  $a \sim 10 - 80 \text{ nm}$ , compared to  $0.1 \text{ nm}$  in  $^4\text{He}$ . As a result only weak surface friction is expected on smooth surfaces, such as sapphire or fused quartz. For our system the expanding/contracting vortex cluster model applies where the essentially rectilinear vortices move in 2-dimensional spiral motion towards the center to form a cluster. The time dependence of the rotation velocity of superfluid component is [69]

$$\frac{d\Omega(t)}{dt} = 2\alpha\Omega(t)[\Omega_r - \Omega(t)], \quad (47)$$

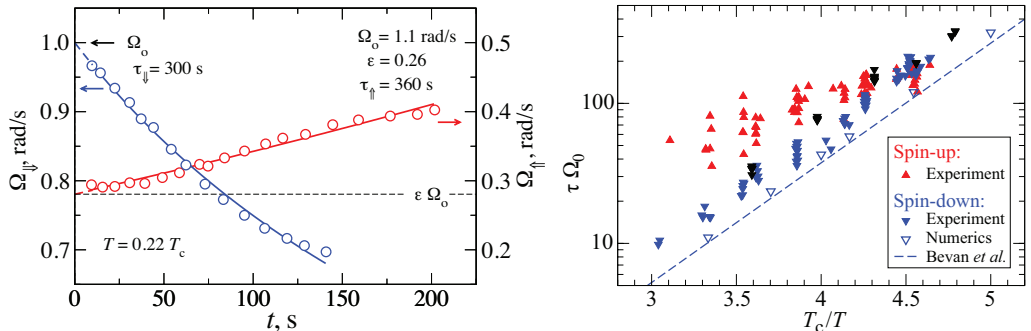


Figure 19: Spin down and spin up experiments on  $^3\text{He-B}$  at  $p = 29$  bar. *Left:* The superfluid vortex flow responses  $\Omega_{\uparrow}$  and  $\Omega_{\downarrow}$  in respectively spin-up and spin-down experiments at  $T = 0.22 T_c$ . Open circles are cf-peak height measurements converted to vortex flow. The calibration of the cf-peak as a function of applied flow is shown in Fig. 1a in publication [P2]. The solid lines are fits using equation (48) and (50). *Right:* Normalized characteristic time constants in terms of  $\tau\Omega_0 = 1/(2\alpha)$  of the vortical flow as a function of inverse temperature. The solid line is an extrapolation of the mutual friction parameter  $\alpha$  from above  $0.35 T_c$ , as measured by Bevan *et al.* [17]. The calculated spin-down simulations are for a cylinder with a tilt  $\eta = 2^\circ$ .

where the drive  $\Omega_r = \Omega_0 u(t)$ , with  $u(t)$  denoting a Heaviside step function. The solution for the response  $\Omega_{\uparrow}$  with the corresponding relaxation time  $\tau_{\uparrow}(T)$  is

$$\Omega_{\uparrow} = \frac{\epsilon\Omega_0}{\epsilon + (1 - \epsilon) \exp(-t/\tau_{\uparrow})}, \quad (48)$$

$$\tau_{\uparrow}(T) = \frac{1}{2\alpha(T)\Omega_0}, \quad (49)$$

where  $\epsilon\Omega_0$  corresponds to the density of vortex lines at  $t = 0$ . In these measurements we used an experimental calibration of the cf-peak dependence on the global flow. Although the NMR signal of the cf-peak decreases rapidly with temperature, by applying enough counterflow by using a large step  $\Delta\Omega$ , the cf-peak is prominent. The left graph in Fig. 19 shows a spin-up measurement where the superfluid velocity increases due to the increasing number of rectilinear vortices.

In the analysis the transformation of the cf-peak to the superfluid flow  $\Omega_{\uparrow}$  is valid, since the counterflow  $v_n - v_s$  during spin-up has solid-body form  $\Omega_{\uparrow}r$ . Both the height and frequency shift of the cf-peak recorded during the spin-up measurements agree with those measured in the calibration, see left graph in Fig. 1 in publication [P2]. The right graph of Fig. 19 shows the characteristic time (49) in spin-up measurements. If the system would have been in a turbulent state, the extra dissipation would have moved the data below the mutual friction line  $\tau\Omega_0 = 1/(2\alpha)$ , which is not observed.

### 5.3 Vortex annihilation

A vortex mediates the interaction between the normal and superfluid components by means of the mutual friction (24). When the fluid is at constant rotation and contains a vortex configuration which is not the equilibrium state, the vortices reorganize the configuration through reconnections within the cluster or annihilation at the surface. Examples of non-equilibrium configurations are randomly distributed remanent vortices and vortex configurations in spin-down experiments. In this section we describe the processes involved during the spin-down of vortex clusters in superfluid  $^3\text{He-B}$  in a variety of geometries. The section is concluded with an experiment where vortices annihilate when the applied flow is reversed, with a remarkable result.

In the zero temperature limit  $T \rightarrow 0$  of superfluid  $^4\text{He}$ , the dynamics of vortices in applied flow was found to be turbulent [36]. The small core radius  $a \approx 0.1\text{nm}$  of the  $^4\text{He}$  vortex lines allows for strong surface pinning. The vortex ends on the surface are not immobile, but less mobile than in the case of  $^3\text{He-B}$ . The vortex core size in  $^3\text{He-B}$  is significantly larger,  $a \sim 10 - 80\text{ nm}$ , which reduces surface pinning, in particular when the surface is smooth as is the case in our experimental cylindrical container.

The spin-down response of  $^3\text{He-B}$ , starting from the equilibrium vortex state, depends on the geometry of the system. Numerical simulations of a vortex cluster in a cubical geometry show that the vortex flow becomes turbulent owing to the large perturbation of the global flow by the corners. Initially, a large overshoot of  $\sim 50\%$  is seen to develop in the vortex length  $L(t)$  when kinetic energy is converted to a turbulent tangle in the bulk volume. Thereafter  $L(t)$  decays with the faster rate  $t^{-3/2}$  as expected for a turbulent response [27] owing to the large reconnection rate in the bulk volume. The turbulence does not develop fully, in the center of the cube the vortices remain comparatively straight. The overall response in the line density  $L(t)$  is shown in Fig. 18 in [P5].

In contrast, the spin-down of the superfluid in spherical and weakly inclined cylindrical geometries is laminar. Here the average line density  $L(t)$  decays monotonically from  $L(0)$ , which is its maximum, with a slower time dependence  $L(t) \propto t^{-1}$ . The expanding vortex cluster model describes the process of the 2-dimensional spiral expanding motion of almost rectilinear vortices, see equation (47), which has the solution

$$\Omega_{\downarrow}(t) = \Omega_0/(1 + t/\tau_{\downarrow}), \quad (50)$$

$$\tau_{\downarrow} = 1/(2\alpha(T)\Omega_0). \quad (51)$$

Fig. 20 shows the decay of the superfluid flow  $\Omega_{\downarrow}$  in a cylinder with a small inclination angle of  $\eta < 1^\circ$  after a rapid deceleration of rotation to zero. The temperature of the fluid corresponds to  $Re_{\alpha} \approx 10^3$ . In this measurement the cf-peak in the NMR spectrum was monitored and later converted to superfluid flow by use of an experimental calibration in the vortex free state. The cf-peak signal vanishes when the counterflow  $\Omega_{\downarrow}$  drops below the critical velocity  $\Omega_{t1}$  (see section 4.1). To measure the superfluid velocity at a later moment, the rotation velocity was increased to  $\Omega_f = 1\text{ rad/s}$  which brought the cf-peak back and allowed one more reading to be added to the decay curve.

A naive argument countering the claim of laminar vortex flow could have been that the signal represents the decay of a Vinen-like random turbulent tangle for which the decay with the same time dependence in the relaxation of the vortex length  $L(t) \propto t^{-1}$ . This argument

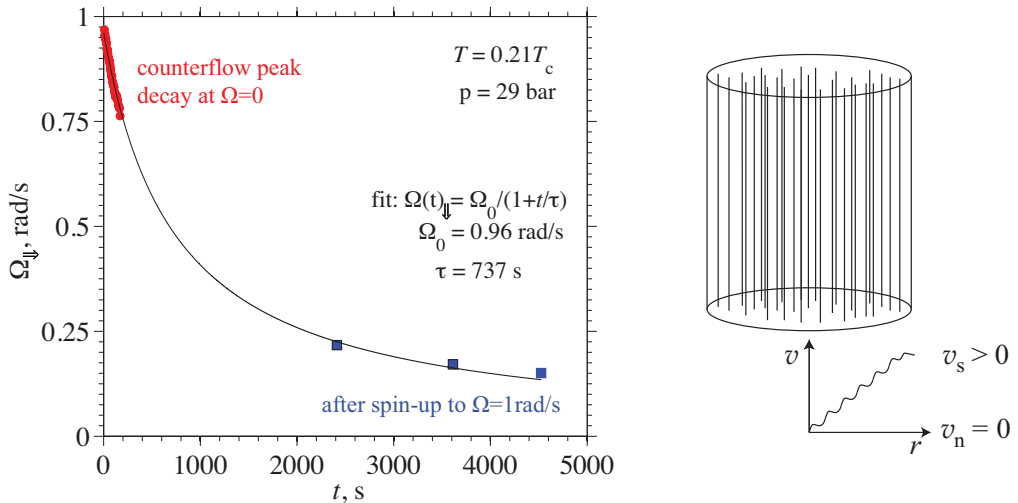


Figure 20: Spin-down experiment at  $T = 0.21 T_c$  and  $p = 29$  bar. *Left*: The equilibrium vortex state is at  $\Omega = 0.98$  rad/s, but is then rapidly decelerated and reaches zero at time  $t = 0$ . The NMR response of the counterflow peak is monitored as a function of time and converted to solid-body-like azimuthal flow  $\Omega_{\downarrow}$ . Owing to the critical velocity  $\Omega_{t1}$ , the cf signal disappears after 3 minutes. At a later moment a fast acceleration of the system to  $\Omega_r = 1$  rad/s recovers the cf signal since  $\Omega_r - \Omega_{\downarrow} > \Omega_{t1}$  and  $\Omega_{\downarrow}$  can be measured. The increase of rotation velocity with the rate  $\dot{\Omega} = 0.03$  rad/s hardly affects the number of vortices. (Compared to the much longer spin-up relaxation time in Fig. 19 right). The experiment is repeated to obtain multiple late time measurements. These correspond to the 3 data points at late time in the tail of the decay curve. *Right*: illustration of an expanding vortex cluster at zero rotation velocity. The homogeneous distribution of the vortices creates a flow profile similar to the a rotating vortex free state, but with opposite sign of the counterflow.

is simply refuted since the NMR signal indicates here a global azimuthal counterflow arising from a decaying solid-body density of vortex lines.

Additional details of the spin-down process can be learned from numerical simulations. In the cylindrical geometry with a small inclined angle ( $\eta = 2^\circ$ ), the vortices in the center are relatively straight and parallel to the rotation axis. However, close to the surface boundary sharp kinks are seen on the reconnecting vortices during the spin-down process and the self induced velocity of the vortices (from the mirror image of each vortex) give rise to a wide range of local velocities and reconnection processes, which amounts to a disordered surface layer for the annihilating vortices. The reconnecting events concentrate within a thin shell adjacent to the cylindrical wall at  $T \approx 0.3 T_c$ , while at  $0.22 T_c$  the width of the layer has grown towards the center of the cylinder. Hence, the unstable boundary layer appears to expand in width with decreasing temperature, but this is not visible in the NMR measurements of the vortices in the bulk. For bulk turbulence to exist in the spin-down measurements, the perturbation from axially symmetric flow is only significant enough at a large inclination

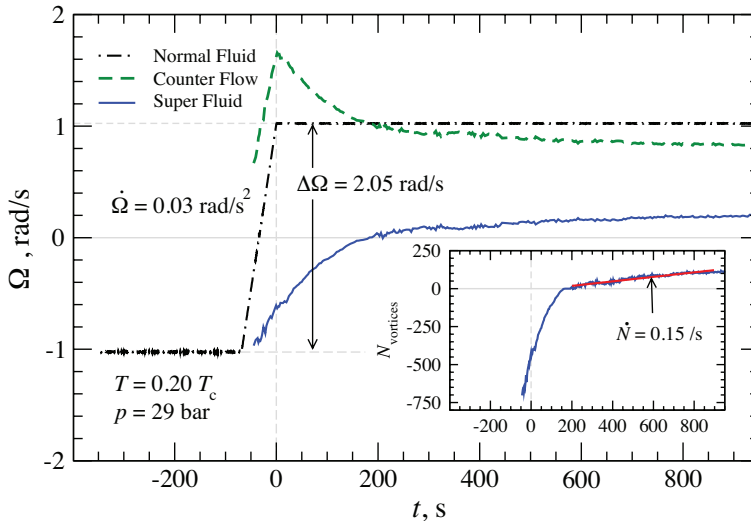


Figure 21: Response of the superfluid flow to a reversal in the rotation direction. The inverted rotation velocity of 1 rad/s is reached at time  $t = 0$  (main panel). First the initial equilibrium vortex state decays slowly in laminar fashion. After a decay of about 3 min the original vortices of wrong polarization are gone and a slow increase in the number vortices at correct orientation starts. New vortices are formed at a slow rate ( $\dot{N} \approx 0.15$  /s) in the single-vortex wall reconnection instability (inset). Finally, a turbulent burst intervenes and a vortex front is observed to propagate through the NMR detection coil.

angle  $\eta$ . At less than  $30^\circ < \eta < 40^\circ$  the flow is still laminar with  $t^{-1}$  time dependence, while above the response is turbulent with  $t^{-3/2}$  time dependence. See Fig. 2c in publication [P2] which demonstrates this transition from laminar to turbulent vortex flow in the bulk volume as a function of the angle  $\eta$ .

The annihilation of vortices is thus laminar in the bulk volume in spin-down experiments with a weakly tilted cylinder, but what happens when the spin-down is followed by spin-up which is accomplished by reversing the rotation velocity from  $+|\Omega|$  to  $-|\Omega|$ ? Do we get turbulence from newly formed vortices at the surface (correctly polarized), which interact with the vortices in the cluster with opposite polarization? The answer is no: the initial vortex cluster expands in laminar flow until full annihilation, with a few exceptions of remnants. These manage to reverse their polarization as short loops, which flip over [75]. The measurement in Fig. 21 shows laminar decay even in this complex process of sudden reversal of the rotation direction. The multiplication process is the single-vortex wall reconnection instability, which lasts for up to 15min before a local burst intervenes.

## 5.4 Propagating superfluid vortex front

In rotating vortex-free counterflow, where the superfluid component is at rest with respect to the laboratory frame and the normal component co-rotates with the cylinder, an injection of vortices at low enough temperature results in a local turbulent burst, as described in section 5.2. The burst has not been observed directly to happen inside a NMR detection coil, presumably because it occurs faster than the sampling time of  $\sim 0.25$  s of our spectrometers. However, the evolution of the spin-up process takes a completely different nature after the burst. In this section we describe the evolution of the moving vortex front and the trailing twisted vortex bundle behind it at temperatures  $T < T_{\text{on}}^{\text{bulk}} \sim 0.59 T_c$ , where the superfluid Reynolds number  $Re_\alpha \geq 1$ .

After the burst, the vortices in the front expand along the axis in spiraling motion into the Landau state, bring the vortex number behind the front close to equilibrium, and thereby dissipate the kinetic energy of the vortex-free flow. See Fig. 22 for a description of the setup. The Landau state is metastable and has a larger free energy than the stable equilibrium vortex state. Hence the front propagation, which takes place with the velocity  $V_f$ , is a direct

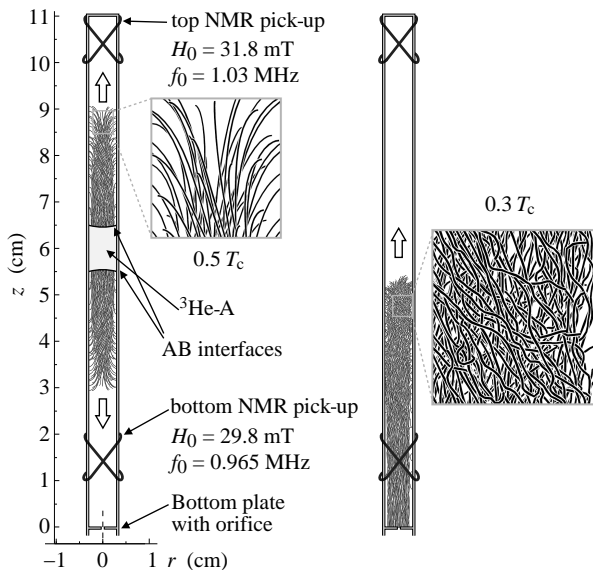


Figure 22: Experimental setup of the vortex front propagation measurements. *Left*: front propagation after vortex injection from the instability of the AB-interface. *Right*: front propagation after an injection of vortices from the orifice. The passage of the front through the NMR coils is seen in the NMR spectrum as a decrease of the cf-peak height, or as a small increase near the Larmor frequency (which reflects the axial flow created by the twist). While above  $\sim 0.4 T_c$  the front thickness increases during the propagation, below this temperature the front thickness is constant at  $\Delta(r) \simeq R$ , the radius of the cylindrical container.

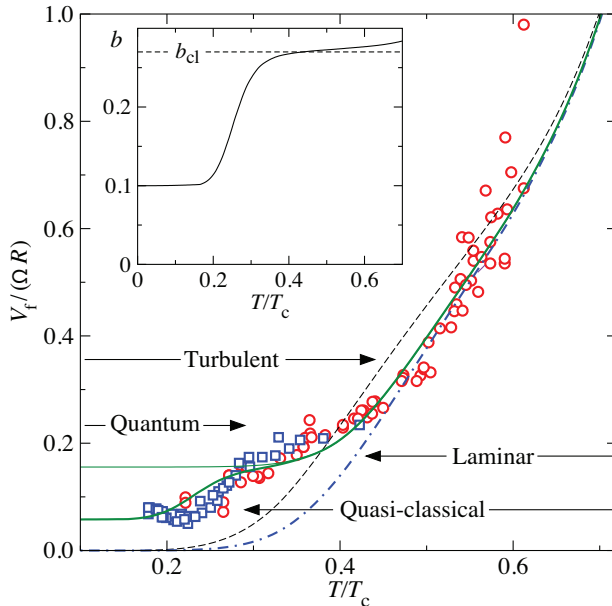


Figure 23: Scaled front propagation velocity versus temperatures. Open circles and squares mark measurements with injection using the AB interface instability and orifice trapping, respectively. The dashed line is the mutual friction coefficient  $\alpha(T)$  [20]. Dash-dotted, thin solid and thick-solid lines show model approximations which sequentially account for dissipation in the large-scale motion, turbulent energy transfer and bottleneck effect. *Inset*: value of parameter  $b(T)$  expressing the drop in the energy flux which was used in producing the thick solid line in the main panel.

measure of the rate of dissipation of the kinetic energy  $\mathcal{E}(t)$ . If one assumes that the vortex state behind the front is the equilibrium state, the rate of dissipation of the kinetic energy is

$$d\mathcal{E}/dt = -\pi\rho_s V_f \Omega^2 R^4 / 4. \quad (52)$$

Earlier measurements by Bradley *et al.* showed that turbulent decay below  $0.2T_c$  was found to be temperature-independent [65]. Our measurements of the front propagation show complex behaviour, which at high temperatures is laminar and depend on the mutual friction parameter  $\alpha(T)$ . At lower temperatures the front propagation velocity is dominated by turbulent dissipation and can be divided into two regimes where the dissipative process changes in nature. Using Fig. 23 as a guide, a discussion of the different behaviours follows:

*Laminar regime*: At high enough temperature ( $\geq 0.4T_c$ ), front propagation is laminar and the front velocity is determined by the mutual friction between the normal and superfluid components:  $V_f \approx \alpha(T)\Omega R$ , where  $\alpha$  is the mutual friction parameter, see section 1.4. The reduced velocity  $v_f = V_f/\Omega R \approx \alpha$  is shown as the dashed line in Fig. 23. In this approximation inter-vortex interactions are ignored. The vortex array behind the front is twisted, due to the

azimuthal motion of the vortices in the front. The helical vortex structure has a wave length which is expected to be proportional to  $q = \frac{V_{L,\phi}}{RV_{L,z}}$ . In the laminar regime the twist behind the front creates axial flow, which gives a slight correction for the front velocity as shown by the dash-dotted line in Fig. 23 [77]. The twist slowly unwinds at the ends of the cylinder where vortices slide over the end plates. The axial flow produced by the twisted cluster is along the vortex expansion direction close to the cylindrical boundary and in the opposite direction close to the axis. In the NMR spectrum, axial flow is reflected by an increase in absorption near the Larmor peak (see Fig. 4 in [P10]). The rate of relaxation of the twist increases with decreasing temperature [77]. Above  $0.46 T_c$  the front thickness  $\Delta$  increases while it propagates into the Landau state. In numerical simulation using the vortex filament model with full Biot-Savart equations and an additional solution of the Laplace equation for solid wall boundary conditions [78], the thickness of the front is  $\Delta(r) \simeq r$ , see left picture of Fig. 22.

*Dissipation anomaly:* Measurements of the front propagation velocity below  $0.4 T_c$  show larger dissipation than expected for laminar propagation. This is similar to the *viscous anomaly* in classical turbulence where the dissipation rate in turbulent flow does not vanish when the viscosity  $\nu$  goes to zero. In superfluid  $^3\text{He-B}$ , we call it the *mutual-friction anomaly* and ascribe it to the turbulent motions in the vortex front.

*Quasi-classical turbulence:* In the quasi-classical turbulent regime, the front propagation velocity  $V_f$  is significantly larger than expected from laminar viscous flow alone. In this regime, the front has become turbulent which increases the dissipation above that expected for laminar mutual-friction-resisted front motion. The contribution to this increase in dissipation is determined by the energy flux in classical turbulence  $\epsilon \simeq bK^{3/2}(\vec{r})/L(\vec{r})$  at an outer scale of turbulence  $L(\vec{r})$ , where  $L(\vec{r}) \simeq \Delta(r)$ , the thickness of the turbulent front as a function of the radius of the cylinder. For the classical Kolmogorov-41 regime,  $b_{cl} \simeq 0.27$  [79]. The contribution to the dissipation by turbulence in the front is seen as a relatively high front propagation velocity compared to the dissipation by laminar viscous flow. In the figure this is shown as a plateau in the propagation velocity. The front velocity  $V_f$  in the zero-temperature limit does saturate to an effective  $\alpha_{\text{eff}} \sim 0.16$  as shown by the thin green line below  $0.3 T_c$ . Influence from the increasing instability of vortex motion at lower temperatures are also seen in the twisted vortex bundle behind the front. The twist reaches a maximum at  $0.45 T_c$  (see Fig. 5 in [P10]), close the transition from laminar to turbulent front propagation. Towards lower temperatures vortices become increasingly unstable and more and more reconnections between the vortices within the bundle contribute to the decrease of the twist.

*Quantum turbulence:* Below  $0.3 T_c$  we observe a decrease of the front velocity with decreasing temperature. Here the energy cascade to length scales is assumed to reach the quantum scale  $\ell$ , owing to the rapidly decreasing mutual friction and the subsequent decrease in dissipation at all length scales. The length-scale  $\ell$  is on the order of the inter-vortex distance. At length-scales comparable to, or smaller than  $\ell$ , vortex discreteness and quantization effects become important and the nonlinearly interacting Kelvin waves dominate the dissipation [27, 85, 86, 87, 88]. Kelvin waves are much less efficient in cascading the energy transfer down scale than classical hydrodynamic turbulence. The latter is suppressed at scales of order  $\ell$ . This is called the bottleneck effect and is reflected by the drop in the

parameter  $b_{cl}$  to  $\simeq 0.1$  for  $T < 0.2T_c$  (see inset of Fig. 23). The improved transfer of energy to smaller length-scales below about  $0.25T_c$ , is seen as the decrease in the propagation velocity of the front below  $0.2T_c$ . The behaviour of the vortex front velocity at all measured temperatures according to the fitted model is shown by the thick (green) line in the main graph of Fig. 23.

The latest measurement of front propagation (not included in this thesis) demonstrates that below  $0.3T_c$  the vortex density in the front and in the trailing twisted bundle, which roughly obey the solid-body-rotation rule, starts to decrease from the equilibrium value with decreasing temperature. This phenomenon is assumed to reflect the growing decoupling of the superfluid component from the reference frame established by the normal component, which at these temperatures is rapidly getting more tenuous. Thus full understanding of the front behaviour in the zero-temperature limit requires further research.

## 6 Conclusions

The motion of vortices in superfluid  $^3\text{He-B}$  becomes inherently unstable below  $0.6 T_c$ , where the superfluid Reynolds number  $Re_\alpha = (1 - \alpha')/\alpha$  exceeds unity due to the rapidly decreasing contribution of the viscous normal component to the mutual friction parameter  $\alpha$ . At the transition temperature  $T_{\text{on}}^{\text{bulk}} = 0.59 T_c$  (at  $p = 29$  bar) the onset to bulk turbulence is seen when a vortex bundle of  $5 - 10$  vortices is injected in the rotating Landau state from the AB-interface. At a slightly lower temperature  $T_{\text{on}}^{\text{wall}}$ , turbulence starts when the single vortex instability takes places repeatedly at the cylindrical surface after increasing the rotation velocity. The process occurs at expanding remanent or seed vortices along the surface of the cylinder, where reconnections of the vortex to the wall lead to slow vortex multiplication. Subsequently, when enough new vortices have been formed a turbulent burst intervenes abruptly. The onset temperature  $T_{\text{on}}^{\text{wall}}$  depends on the applied flow and the number of vortices connected to the cylindrical surface. Although both transitions are stochastic in nature, the width of the transition is sharp. Our smooth-walled container shows no preferred location for the turbulent burst to occur, which we interpret to mean that (with the exception of the neighbourhood of the orifice) there are no isolated strong pinning sites on the container walls.

What happens after a local turbulent burst in the rotating superfluid? The ends of the vortices on the cylindrical surface move in helically spiral motion and dissipate the kinetic energy of the meta-stable Landau state. The spiraling motion of the vortices creates a twisted state behind the front, which induces axial flow. In the laminar regime ( $> 0.4 T_c$ ) the thickness of the front (measured along the cylinder axis) increases during the propagation, while at lower temperatures the thickness is constant. Below  $0.4 T_c$  the front becomes turbulent, which increases the dissipation compared to that in laminar flow. However, below  $0.3 T_c$  the energy cascade at length scales comparable to the inter-vortex spacing becomes important. Here the transfer of kinetic energy to shorter length scales by the Kelvin waves is much smaller than the transfer of the energy in quasiclassical Kolmogorov turbulence. The resulting pile-up of energy at the length-scale of the inter-vortex distance is called the bottleneck effect and is experimentally observed as a plateau-like leveling off of the front velocity as a function of temperature.

With decreasing temperature the damping of the vortex motion decreases and turbulence was expected to become more prevalent. This is not the case for the dynamic responses in a cylindrically symmetric rotating container. We observe laminar global flow in spin-up experiments if the cylinder originally contained a roughly uniform distribution of remanent vortices. In the applied flow these remanent vortices expand along the axis on the cylindrical surface and create new independent vortex loops when the vortices reconnect to the surface. Rectilinear vortices are formed when these expanding vortices reconnect to each other. The now polarized vortices spiral in a laminar motion towards the center of the container and form a cluster. Laminar motion of vortices is also seen in spin-down experiments where the equilibrium vortex cluster expands after the rotation velocity of the container has been stopped abruptly. Only vortices adjacent to the container surface create a thin layer of turbulence when the Kelvin waves and kinks on the annihilating vortices reconnect to the surface. At temperatures where the superfluid Reynolds number  $Re_\alpha \sim 10^3$ , the laminar motion of vortices was not expected, since experiments in superfluid  $^4\text{He}$  show always turbulent

behaviour under similar conditions. Numerical simulations show that superfluid  $^3\text{He-B}$  can become turbulent when the geometry of the container deviates strongly from axial symmetry or the tilt of the cylinder from the rotation axis is appreciable ( $> 35^\circ$ ).

The measured NMR line shapes of rotating superfluid  $^3\text{He-B}$  at a variety of rotation velocities and cluster configurations agree with numerical calculations using the hydrostatic theory of superfluid  $^3\text{He-B}$ . This allows the extraction of the density anisotropy parameter  $\lambda_{\text{HV}}$ . Analysis of the density anisotropy shows that the value for the energy gap in the zero-temperature limit is higher than predicted by *weak-coupling plus theory*, and confirms earlier measurements by Todoshchenko *et al.* The measured phase diagram of the flare out textures show that the rotation velocity at which the counterflow peak appears, increases rapidly with decreasing temperature. At the magnetic field of  $\sim 61$  mT at  $0.2 T_c$ , the cf-peak appears above the rotation velocity  $\Omega_{\text{t1}} \sim 0.9$  rad/s, which is experimentally feasible to reach under those conditions. The transition between the *parted* and *extended* flare out textures occurs at higher rotation velocities. Here the transitions show a large hysteresis in terms of rotation velocity, and to a lesser extent also in temperature. The hysteresis in rotation velocity increases rapidly beyond 2 rad/s. Measurements on the static susceptibility agree with extrapolations of earlier measurements and confirm the currently accepted value of the Fermi-liquid parameter  $F_0^a$ .

Quartz tuning forks with a high quality factor have been investigated and found to be excellent tools for low temperature measurements where the superfluid is in the ballistic regime. This is important since the temperature-dependent longitudinal Leggett frequency is practically saturated below  $0.3 T_c$  and the melting curve thermometer loses thermal contact with the  $^3\text{He-B}$  sample. The extreme sensitivity of the fork in temperature measurements allows to study Andreev reflection of quasiparticles from vortex tangles or to perform bolometric measurements of vortex front motion.

# Appendix

A complete list of publications in which the author participated (date sorted).

1. J.J. Hosio, V.B. Eltsov, R. de Graaf, M. Krusius, J. Mäkinen and D. Schmoranzer, arXiv:1103.2633v1 [cond-mat.other] (2011)
2. V.B. Eltsov, R. de Graaf, J.J. Hosio, P.J. Heikkinen, R. Hänninen, M. Krusius, V.S. L'vov, G.E. Volovik, arXiv:1102.4284v1 [cond-mat.other] (2011)
3. R. de Graaf, V.B. Eltsov, J.J. Hosio, P.J. Heikkinen and M. Krusius, J. Low Temp. Phys. (Accepted February 16, 2011)
4. V.B. Eltsov, R. de Graaf, M. Krusius and D.E. Zmeev, J. Low Temp. Phys. **162**, 212225 (2011)
5. V.B. Eltsov, R. de Graaf, P.J. Heikkinen, J.J. Hosio, R. Hänninen and M. Krusius, J. Low Temp. Phys. **161**, 474-508 (2010)
6. V.B. Eltsov, R. de Graaf, P.J. Heikkinen, J.J. Hosio, R. Hänninen, M. Krusius and V.S. L'vov, Phys. Rev. Lett. **105**, 125301 1-4 (2010)
7. Yu.M. Bunkov, V.B. Eltsov, R. de Graaf, P.J. Heikkinen, J.J. Hosio, M. Krusius and G.E. Volovik, arXiv:1002.1674v1 [cond-mat.quant-gas] (2010)
8. R. Hänninen, V.B. Eltsov, A. Finne, R. de Graaf, J. Kopu, M. Krusius and R. Solntsev, J. Low Temp. Phys. **155** (1-2), 98-113 (2009)
9. V.B. Eltsov, R. de Graaf, R. Hänninen, M. Krusius and R.E. Solntsev, J. Low Temp. Phys. **150** (3-4), 373-383 (2008)
10. V.B. Eltsov, R. de Graaf, R. Hänninen, M. Krusius, R.E. Solntsev, V.S. L'vov, A.I. Golov and P. Walmsley, Prog. Low Temp. Phys. **XVI**, 45 (2008)
11. M. Blažková, M. Človečko, V.B. Eltsov, E. Gažo, R. de Graaf, J.J. Hosio, M. Krusius, D. Schmoranzer, W. Schoepe, L. Skrbek, P. Skyba, R.E. Solntsev and W.F. Vinen, J. Low Temp. Phys. **150** (3-4), 525-535 (2008)
12. R. de Graaf, R. Hänninen, T.V. Chagovets, V.B. Eltsov, M. Krusius and R.E. Solntsev, J. Low Temp. Phys. **153** (5-6), 197-227 (2008)
13. R.E. Solntsev, R. de Graaf, V.B. Eltsov, R. Hänninen and M. Krusius, J. Low Temp. Phys. **148** (3-4), 311-316 (2007)
14. R. Blaauwgeers, M. Blažková, M. Človečko, V.B. Eltsov, R. de Graaf, J.J. Hosio, M. Krusius, D. Schmoranzer, W. Schoepe, L. Skrbek, P. Skyba, R.E. Solntsev and D.E. Zmeev, J. Low Temp. Phys. **146** (5-6), 537-562 (2007)
15. V.B. Eltsov, A.I. Golov, R. de Graaf, R. Hänninen, M. Krusius, V.S. L'vov and R.E. Solntsev, Phys. Rev. Lett. **99** (26), 265301 1-4 (2007)

## References

- [1] E.M. Lifshitz and L.P. Pitaevskii, *Statistical Physics part 2, Landau and Lifshitz course of Theoretical physics*, Pergamon Press, Oxford, UK (1980)
- [2] J. Bardeen, L.N. Cooper and J.R. Schrieffer, Phys. Rev. **108**, 1175 (1957)
- [3] P.W. Anderson and W.F. Brinkman, Phys. Rev. Lett. **30**, 1108 (1973)
- [4] R. Balian and N.A. Werthamer, Phys. Rev. **131**, 1553 (1963)
- [5] D. Vollhardt and P. Wölfle, *The Superfluid Phases of Helium 3*, Taylor & Francis, London, UK (1990)
- [6] P.J. Hakonen, M. Krusius, M.M. Saloma, R.H. Salmelin and J.T. Simola, J. Low Temp. Phys. **76**, 225 (1989)
- [7] E.V. Thuneberg, J. Low Temp. Phys. **122**, 213 (2001)
- [8] A.J. Leggett, Ann. Phys. **85**, 11 (1974)
- [9] J. Kopu, R. Schanen, R. Blaauwgeers, V.B. Eltsov, M. Krusius, J.J. Ruohio and E.V. Thuneberg, J. Low Temp. Phys. **120**, 213 (2000)
- [10] E.R. Dobbs, *Helium Three*, Oxford University Press, New York, USA (2000)
- [11] J. Kopu, J. Low Temp. Phys. **146**, 47 (2007)
- [12] D.R. Tilley and J. Tilley, *Superfluidity and superconductivity*, IOP Publishing, Bristol, UK (1990)
- [13] L. Onsager, Nuovo Cimento **6**, 249 (1949)
- [14] R. Feynman, Progr. Low Temp. Phys. **1**, 17, North Holland, Amsterdam, NL (1955)
- [15] E.V. Thuneberg, Phys. Rev. Lett. **56**, 359 (1986)
- [16] Y. Kondo, J.S. Korhonen, M. Krusius, V.V. Dmitriev, E.V. Thuneberg and G.E. Volovik, Phys. Rev. Lett. **68**, 3331 (1992)
- [17] T.D.C. Bevan, A.J. Manninen, J.B. Cook, H. Alles, J.R. Hook and H.E. Hall, J. Low Temp. Phys. **109**, 423 (1997)
- [18] G.A.C.M. Spiering, J. Mater. Sci. **28**, 6261 (1993)
- [19] R.J. Donnelly, *Quantized Vortices in Helium II*, Cambridge University Press, Cambridge, UK (1991)
- [20] T.D.C. Bevan, A.J. Manninen, J.B. Cook, H. Alles, A.J. Armstrong, J.R. Hook and H.E. Hall, Phys. Rev. Lett. **74**, 750 (1995)

- [21] N.B. Kopnin, Rep. Prog. Phys. **65**, 1633 (2002)
- [22] A.R. Paterson, *A First Course in Fluid Dynamics*, Cambridge University Press, Cambridge, UK (1983)
- [23] L.D. Landau and E.M. Lifshitz, *Fluid Mechanics*, Pergamon Press, Oxford, UK (1987)
- [24] T.E. Faber, *Fluid Dynamics for Physicist*, Cambridge University Press, Cambridge, UK (1995)
- [25] B. Hof, A. Juel and T. Mullin, Phys. Rev. Lett. **91**, 244502 (2003)
- [26] A.N. Kolmogorov, Dokl. Akad. Nauk. SSSR **30**, 299 (1941)
- [27] W.F. Vinen and J.J. Niemela, J. Low Temp. Phys. **128**, 167 (2002)
- [28] S.N. Fisher, A. Hale, A.M. Guénault and G.R. Pickett, Phys. Rev. Lett. **86**, 244 (2001)
- [29] D.I. Bradley, S.N. Fisher, A.M. Guénault, M.R. Lowe, G.R. Pickett and A. Rahm, J. Low Temp. Phys. **124**, 113 (2001)
- [30] D.I. Bradley, S.N. Fisher, A.M. Guénault, M.R. Lowe, G.R. Pickett, A. Rahm and R.C.V. Whitehead, Phys. Rev. Lett. **93**, 235302 (2004)
- [31] V.M.H. Ruutu, Ü. Parts, J. Koivuniemi, N.B. Kopnin and M. Krusius, J. Low Temp. Phys. **107**, 93 (1997)
- [32] A.P. Finne, S. Boldarev, V.B. Eltsov and M. Krusius, J. Low Temp. Phys. **136**, 249 (2004)
- [33] A.P. Finne, S. Boldarev, V.B. Eltsov and M. Krusius, J. Low Temp. Phys. **138**, 567 (2005)
- [34] A.P. Finne, V.B. Eltsov, G. Eska, R. Hänninen, J. Kopu, M. Krusius, E.V. Thuneberg and M. Tsubota, Phys. Rev. Lett. **96**, 085301 (2006)
- [35] P.M. Walmsley, A.A. Levchenko and A.I. Golov, J. Low Temp. Phys. **145**, 143 (2006)
- [36] P.M. Walmsley, A.I. Golov, H. Hall, A. Levchenko and W. Vinen, Phys. Rev. Lett. **99**, 265302 (2007)
- [37] P.M. Walmsley and A.I. Golov, Phys. Rev. Lett. **100**, 245301 (2008)
- [38] J.S. Korhonen, A.D. Gongadze, Z. Janú, Y. Kondo, M. Krusius and E.V. Thuneberg, Phys. Rev. Lett. **65**, 1211 (1990)
- [39] M.M. Salomaa, J. Phys.: Condens. Matter **2**, 1325 (1990)
- [40] J.P. Davis, H. Choi, J. Pollanen and W.P. Halperin, J. Low Temp. Phys. **153**, 1 (2008)
- [41] I.A. Todoshchenko, H. Alles, A. Babkin, A.Y. Parshin and V. Tsepelin, J. Low Temp. Phys. **126**, 1449 (2002)

- [42] J.S. Korhonen, Y.M. Bunkov, V.V. Dmitriev, Y. Kondo, M. Krusius, Y.M. Mukharskiy, Ü. Parts and E.V. Thuneberg, *Phys. Rev. B* **46**, 13983 (1992)
- [43] R. Blaauwgeers, Doctoral Thesis, Leiden University, NL (2001)
- [44] A. Finne, Doctoral Thesis, Helsinki University of Technology, FI (2005)
- [45] *Digital Precision Electronic Positioning System*, Technical Manufacturing Corporation, 15 Centennial Drive, Peabody, MA 01960, USA. The control unit is PEPS II.
- [46] *High resolution optical encoder*, GES Group, Humboldtstrasse 11, 78549, Spaichingen, Germany. The unit is model LH120.
- [47] *High-Q surface mount capacitors*, Spectrum Control Inc. 6000 West Ridge Road, Erie, PA 16506, U.S.A.
- [48] V.B. Eltsov, R. de Graaf, J.J. Hosio, P.J. Heikkinen, R. Hänninen, M. Krusius, V.S. L'vov and G.E. Volovik, arXiv:1102.4284v1 [cond-mat.other] (2011)
- [49] P.J. Heikkinen, Diploma Thesis, Aalto University, School of Science and Technology, FI (2010)
- [50] E.L. Andronikashvili, *J. Phys. USSR* **10**, 201 (1946)
- [51] E.L. Andronikashvili, *Zh. Eksp. Teor. Fiz.* **18**, 424 (1948)
- [52] E.L. Andronikashvili, *Prog. Low Temp. Phys.* **5**, 79 (1967)
- [53] M. Niemetz, H. Kerscher and W. Schoepe, *J. Low Temp. Phys.* **126**, 287 (2002)
- [54] W. Schoepe, *Phys. Rev. Lett.* **92**, 095301 (2004)
- [55] H.A. Nichol, L. Skrebek, P.C. Hendry and P.V.E. MacClintock, *Phys. Rev. Lett.* **92**, 244501 (2004)
- [56] H.A. Nichol, L. Skrebek, P.C. Hendry and P.V.E. MacClintock, *Phys. Rev. E* **70**, 056307 (2004)
- [57] H. Yano, A. Handa, H. Nakagawa, K. Obara, O. Ishikawa, T. Hata and M. Nakagawa, *J. Low Temp. Phys.* **138**, 561 (2005)
- [58] D.I. Bradley, D.O. Clubb, S.N. Fisher, A.M. Guénault, R.P. Haley, C.J. Matthews, G.R. Pickett, V. Tsepelin and K. Zaki, *Phys. Rev. Lett.* **95**, 035302 (2005)
- [59] D.I. Bradley, *Phys. Rev. Lett.* **84**, 1252 (2000)
- [60] J. Martikainen, J. Tuoriniemi, T. Knuuttila and G. Pickett, *J. Low Temp. Phys.* **126**, 139 (2002)
- [61] C.B. Winkelmann, E. Collin, Yu. M. Bunkov and H. Godfrin, *J. Low Temp. Phys.* **135**, 3 (2004)

- [62] D.C. Carless, H.E. Hall and J.R. Hook, *J. Low Temp. Phys.* **50**, 583 (1983)
- [63] S.N. Fisher, A.M. Guénault, C.J. Kennedy, and G.R. Pickett, *Phys. Rev. Lett.* **63**, 2566 (1989)
- [64] C. Bäuerle, Yu. M. Bunkov, S. N. Fisher and H. Godfrin, *Phys. Rev. B* **57**, 14381 (1998)
- [65] D.I. Bradley, D.O. Clubb, S.N. Fisher, A.M. Guéneult, R.P. Haley, C.J. Matthews, G.R. Pickett, V. Tsepelin and K. Zaki, *Phys. Rev. Lett.* **96**, 035301 (2006)
- [66] W.F. Brinkman, H. Smith, D.D. Osheroff and E.I. Blount, *Phys. Rev. Lett.* **33**, 624 (1974)
- [67] Yu.M. Bunkov, V.B. Eltsov, R. de Graaf, P.J. Heikkinen, J.J. Hosio, M. Krusius and G.E. Volovik, Arxiv:1002.1674v1 [cond-mat.quant-gas] (2010)
- [68] P.W. Adams, M. Cieplak and W.I. Glaberson, *Phys. Rev. B* **32**, 171 (1985)
- [69] E.B. Sonin, *Rev. Mod. Phys.* **59**, 87 (1987)
- [70] T.W.B. Kibble, arXiv:cond-mat/0211110 (2002)
- [71] V.M.H. Ruutu, V.B. Eltsov, A.J. Gill, T.W.B. Kibble, M. Krusius, Yu.G. Makhlin, B. Plaçais, G.E. Volovik and X. Wen, *Nature* **382**, 334 (1996)
- [72] C. Bäuerly, Yu.M. Bunkov, S.N. Fisher, H. Godfrin and G.R. Pickett, *Nature* **382**, 332 (1996)
- [73] V.B. Eltsov, M. Krusius and G.E. Volovik, *Prog. Low Temp. Phys* **XV**, Elsevier, Amsterdam, NL (2005); preprint arxiv:cond-mat/9809125v4 (2004)
- [74] A.P. Finne, S. Boldarev, V.B. Eltsov and M. Krusius, *J. Low Temp. Phys* **135**, 479 (2004)
- [75] V.B. Eltsov, R. de Graaf, R. Hänninen, M. Krusius, R.E. Solntsev, V.S. L'vov, A.I. Golov and P.M. Walmsley, *Prog. Low Temp. Phys*, **XVI**, Elsevier, Amsterdam, NL (2008), preprint: arXiv:0803.3225v2 (2008)
- [76] A.P. Finne, V.B. Eltsov, R. Blaauwgeers, Z. Janu, M. Krusius and L. Skrbek, *J. Low Temp. Phys.* **134**, 375 (2004)
- [77] V.B. Eltsov, A.P. Finne, R. Hänninen, J. Kopu, M. Krusius, M. Tsubota and E.V. Thuneberg, *Phys. Rev. Lett.* **96**, 215302 (2006)
- [78] R. Hänninen, A. Mitani and M. Tsubota, *J. Low Temp. Phys.* **138**, 589 (2005)
- [79] V.S. L'vov, I. Procaccia and O. Rudenko, *JETP Lett.* **84**, 62 (2006)
- [80] H.E. Hall, *Adv. Phys.* **9**, 89 (1960)
- [81] E.L. Andronikashvili and J.S. Tsakadze, *Zh. Eksp. Teor. Fiz.* **37**, 322 (1959)

- [82] K.L. Henderson and C.F. Barenghi, *Europhys. Lett.* **67**, 56 (2004)
- [83] V.K. Tkachenko, *Zh. Eksp. Teor. Fiz.* **50**, 1573 (1966)
- [84] I. Coddington, P. Engels, V. Schweikhard and E.A. Cornell, *Phys. Rev. Lett.* **91**, 100402 (2003)
- [85] E.V. Kozik and B.V. Svistunov, *Phys. Rev. Lett.* **92**, 035301 (2004)
- [86] W.F. Vinen, *Phys. Rev. B* **61**, 1410 (2000)
- [87] W.F. Vinen, M. Tsubota and A. Mitani, *Phys. Rev. Lett.* **91**, 135301 (2003)
- [88] B.V. Svistunov, *Phys. Rev. B* **52**, 3647 (1995)
- [89] E. Kozik and B. Svistunov, *arXiv:cond-mat/0703047* (2007)
- [90] V.S. L'vov, S.V. Nazarenko and O. Rudenko, *Phys. Rev. B* **76**, 024520 (2007)



ISBN: 978-952-60-4108-7 (pdf)  
ISBN: 978-952-60-4107-0  
ISSN-L: 1799-4934  
ISSN: 1799-4942 (pdf)  
ISSN: 1799-4934

**Aalto University**  
**School of Science**  
**Low Temperature Laboratory**  
[www.aalto.fi](http://www.aalto.fi)

**BUSINESS +  
ECONOMY**

**ART +  
DESIGN +  
ARCHITECTURE**

**SCIENCE +  
TECHNOLOGY**

**CROSSOVER**

**DOCTORAL  
DISSERTATIONS**